Nonlinear Observers for Integrated INS/GNSS Navigation

Implementation Aspects

Torleiv H. Bryne, Jakob M. Hansen, Robert H. Rogne, Nadezda Sokolova,

Thor I. Fossen and Tor A. Johansen

POC: T.H. Bryne (torleiv.h.bryne@itk.ntnu.no)

July 25, 2016

Navigation is a term with broad usage in everyday life, purporting the act of moving, finding one's way in an unknown environment, ascertaining a craft's position or even browsing the pages of the internet. Originally the term meant the skill of sailing a ship, in particular steering and maneuvering, and is derived from the Latin words *navis* and *agere*, translated to "ship" and "to drive". The modern field of study of navigation in a scientific context usually relates to the ascertainment or determination of position, velocity and orientation of some object relative to a reference point, and is used for all type of crafts and vehicles, such as aircraft, ship, submarines and cars.

Before the advent of motion sensors, rotation sensors, computers and electronic navigational aids, navigation at sea was carried out with sextant and, at the time, accurate clocks to manually obtain, measure and calculate the position on Earth. Also, by crudely estimating the ship's speed and heading, the current position could be calculate based on a previously known one, a process referred to as dead reckoning. In the present day, inertial navigation systems (INS) provide the user with position, velocity and attitude (PVA) information with high resolution independent of the vehicle platform. Strapdown INS is a type of INS based on accelerometer and angular rate measurements from sensors mounted directly to the craft's hull or fuselage, while the rotational and translational motion of the craft, relative to the Earth, is obtained through software by mechanization of the strapdown equations in a dead reckoning fashion. Commercially available navigational aids based on global navigation satellite systems (GNSS), in particular the Global Positioning System (GPS), paved the way for wide spread INS utilization based on low-cost inertial sensors, which are in need of frequent position corrections and aiding. For the interested reader, an overview of GNSS and its history is found in "History of Global Navigation Satellite Systems". INS corrections are usually performed using an estimator, where the extended Kalman filter (EKF) traditionally has been the applied estimator, which has been covered in the literature

for five decades, such as in [1]–[5].

As a consequence of increased use of inertial sensor technology, due to price and size reduction combined with increased sensor quality in the last three decades, nonlinear observers (NLOs) for PVA estimation based on inertial sensors with aiding from position and/or velocity measurement systems have been developed. Such results focus on the deterministic estimator's stability properties, usually designed by employing Lyapunov-based stability theory. This is in contrast to stochastic estimators such as the EKF, the multiplicative extended Kalman filter (MEKF), [6], and the unscented Kalman filter (UKF), [7], which is based on approximate minimum variance filtering. Another estimator utilized to solve the navigation problem, also being very different to those based on stability theory, is the particle filter (PF), [8], where a set of chosen particles are used to approximate the posterior distribution of some random pro,cess, in this case the navigation system where the sensor measurements are corrupted with noise.

The results of [9]–[17] are examples of NLOs covering various aspects of navigation. Part of the motivation for research on NLOs is to provide a navigation solution using algorithms that are alternative to the industry standard solutions based on EKF [2]–[5], MEKF, [6], and other Bayesian estimators, in order to be able to theoretically guarantee robustness. Regarding navigation systems for autonomous platforms and new consumer-grade applications, another objective that arises is the reduction of the computational load of the navigation solution. Such reduction might enable the use of small-size and lightweight computational units with reduced arithmetic resolution compared to industry standard navigation computers. The reduction of the navigation computer is beneficial in that more space, weight, energy and power is available for any payload the user wishes the autonomous platform to be equipped with. Compared to stochastic methods, in particular the PF, due to the number of particle needed to correctly approximate the posterior distribution, NLOs has the advantage of having less computational burden.

In the works of [9]–[17], except from [13], fixed observer feedback gains are sufficient to achieve certain stability properties, which guarantee a high degree of robustness. A relevant question, also when comparing NLOs to estimators such as the MEKF and minimum energy filters [18], whose global stability properties are difficult to guarantee, is whether a fixed gain strategy incurs a loss of estimation accuracy in steady-state or transient conditions. If so, an other question needs to be resolved; that is how nonlinear or time-varying gains can be synthesized to achieve significantly better performance of NLOs compared to applying a fixed-gain approach.

Since NLOs are commonly designed using nonlinear stability theory in continuous time, another challenge is how to best discretize the observer dynamics and how to manage

measurements that may have different sampling rates, may be asynchronous, or delayed. For the complementary filter [11], applied to attitude estimation, some answers are given in [19]. For the update of position and velocity estimates, the best practice appears to be use of a corrector–predictor algorithm [20, Ch. 11.3.4], similar to the propagation update steps in a Kalman filter (KF), [21, Ch. 4.2]. Similar ideas can be used to deal with delayed measurements, when the delay is known, [22]–[24]. Still, a systematic study on discrete-time implementation has not been made in the context of NLOs.

The relatively mature literature on EKF for integrated inertial navigation, [2]–[5], has a strong focus on the modeling and estimation of systematic errors such as ionospheric and tropospheric influences on satellite navigation accuracy, and bias and drift characteristics of inertial sensors. In contrast, NLOs typically make no explicit assumptions on the characteristics of such errors, except including "constant parameter" augmentations to estimate the gyro biases, [9]–[17]. It is however clear that the underlying deterministic modeling framework, which the design of NLOs is based upon, could allow some frequency-dependent characterization of sensor errors to be included. By doing so, the INS/GNSS accuracy is potentially increased. In the situation of non-ideal GNSS conditions, some work has been done in [25], applying NLOs to detect GNSS drift which could be caused by receiver clock error, multipath or erroneous differential correction. However, the main focus of this article is on normal GNSS conditions and how NLOs can be designed to obtain accurate position, velocity and attitude estimates.

Application Example

With new emerging technologies, the commercial market for unmanned aerial vehicles (UAV) is growing rapidly. These types of aircraft perform a multitude of task, including surveillance, scientific measurements, environmental monitoring and wildlife mapping, and inherently require an accurate, precise, lightweight and small-size navigation solution. A photograph of a Penguin B fixed-wing UAV is shown in Fig. 1, and its technical specifications are included in Table 1.

In flight, high resolution PVA and temporal information must be provided by the navigation system for the UAV and its operator to safely and accurately control the vehicle and georeference the payload sensor data in order to fulfill the mission objective. At an altitude of 200 m, a $1°$ error in roll corresponds to approximately 3.5 m georeferencing error on the ground, and a 100 ms timing error results in a 3 m error at a speed of 30 m/s. Also, position information obtained from a typical commercial grade GNSS receiver only provide position data at 1–5 Hz, while the dynamics of the craft are much faster than that. Hence, even though GNSS solutions are improving, there are still issues, prompting the employment of integrated GNSS/INS to conduct

Figure 1: Penguin B unmanned aerial vehicle (UAV) in flight. Photo: Jakob M. Hansen.

TABLE 1: Penguin B Unmanned Aerial Vehicle (UAV) Technical Specifications

Engine type:	Gasoline
Wingspan:	3.3 m
Length:	2.27 m
MTOW:	21.5 kg
Endurance:	5+ hours
Cruise speed:	28 m/s
Max level speed:	36 m/s

UAV missions. Moreover, attitude information is also not available using only one GNSS antenna, meaning that this has to be estimated using integrated GNSS/INS. Fig. 2 presents the flight path of a UAV test flight, conducted from Eggemoen, Norway.

In the setup used for validation in this article, the UAV is equipped with an ADIS 16488

4

inertial measurement unit (IMU) measuring specific force, rotation rate and magnetic field of the vehicle at 410 Hz. For more on IMUs, see section "Inertial and Magnetic Measurements" and "Inertial Measurement Units" Additionally a u-Blox LEA-6T GNSS receiver supplies computed position as well as pseudoranges at 5 Hz. The sensors are synchronized using a microcontroller in order to accurately timestamp the measurements. Engine induced vibrations are significant and can typically be seen as a signal of magnitude close to 1 m/s^2 at 70 Hz on the accelerometer measurements.
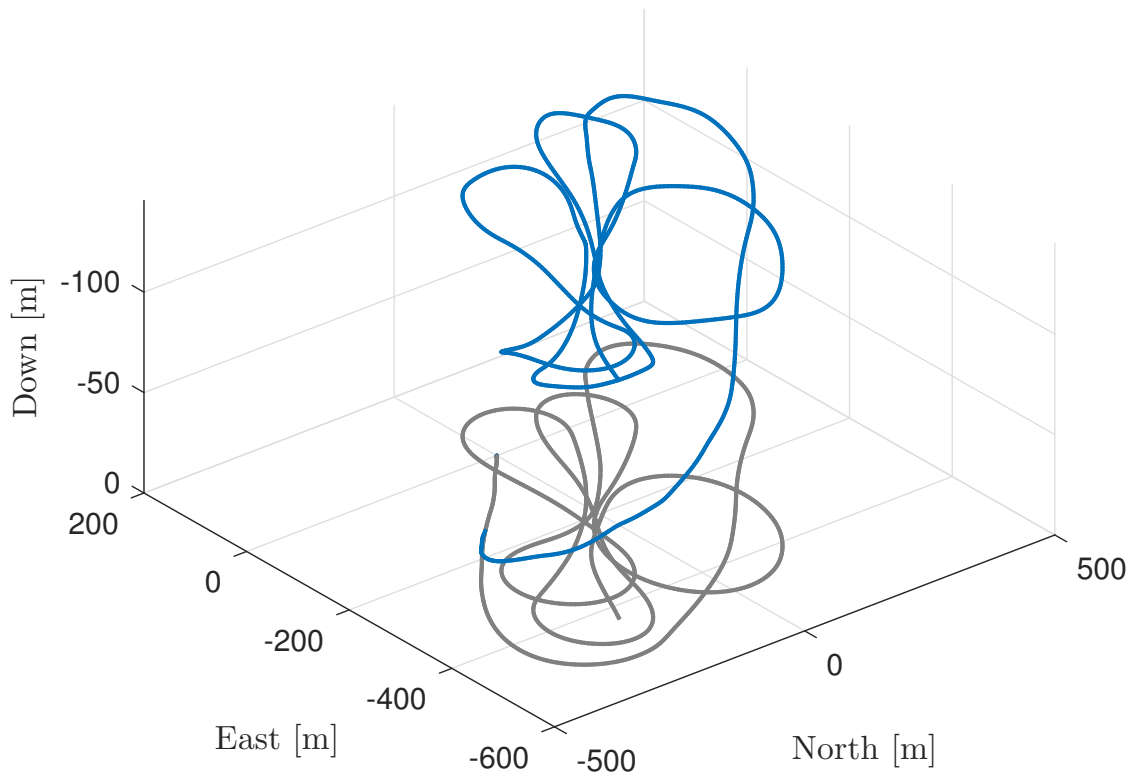

Figure 2: Flight path. The flight path using a Penguin B Unmanned Aerial Vehicle (UAV) is shown. Takeoff of the UAV is used as the origin. The flight path is shown in blue, while the ground track is shown in gray.

Main Contribution

This article considers the NLOs of [16] and [26], which are based on complementary filtering for attitude estimation, [11], in combination with a linear approach to design a translational motion observer (TMO), [27], which in turn is used to estimate the position, linear velocity and specific force. For a conceptual overview, "Complementary Filtering" can be advised. In applied usage, NLOs are immature, in particular related to implementation aspects and

5

handling imperfect measurements with different errors, resolution and sample rates. In addition to present implementation related aspects of the NLO, further re-design is addressed to answer the research questions presented above. The basis for this work include linear methods for exact discretization of the translational motion part of the observer, error model augmentation, and the methods in [19], [20] for discretization, tuning and multi-rate implementation of the attitude observer. Based on this, the main contributions of this articles are:

- A linear time-varying (LTV) representation of the observer error dynamics is exploited to formulate a time-varying Riccati equation to select time-varying gains in the update of velocity and position estimates (as well as some auxiliary variable estimates).
- Strategies originally developed for the Kalman filter are exploited in handling sequential single-measurement updates to accommodate multi-rate and asynchronous measurements in estimation of position, velocity and attitude based both direct and indirect observer implementations.
- Inclusion of GNSS error models in order to take into account the dynamic noise characteristic of GNSS observables.
- Experimental verification of the presented methods using data collected during a unmanned aerial vehicle (UAV) test flight mission.

Organization

The article is organized by first presenting the necessary mathematical notations and definitions. Then, the kinematic modeling, which the INSs are based upon, and the respective inertial sensor models are presented. After that, an overview of the nonlinear observer structures are presented before going into detail by presenting the attitude observer. The presentation follows with the two TMOs, estimating the position, linear velocity and specific forces. The TMO required for the loosely coupled integration scheme is presented first, then the tightly coupled GNSS/INS integration scheme is presented, both with the respective GNSS noise and error models. The experimental verification of the presented methods and algorithms concludes the article.

Notation and Preliminaries

The Euclidean vector norm is denoted as $\| \cdot \|_2$. The column vector $(z_1; z_2)$ describes the vector z_1 stacked over the vector z_2. The set $\mathcal{I}_k$ is a set containing the indices of available measurements at time $t = k \cdot T$ where T indicates the sampling interval and k is the time index. $E[\cdot]$ denotes statistical expectation, while the exponential function is denoted $\mathrm{e}^{(\cdot)}$. The identity matrix of dimension n is denoted I_n, and $0_{n \times n}$ symbolizes a $n \times n$ matrix of zeros, or just 0

where the dimensions are implicitly given by the context. To simplify the notation, usually the time dependency is implicitly given.

A unit quaternion $q = (s_q; r_q)$ with $||q||_2 = 1$ consists of a real part $s_q \in \mathbb{R}$ and a vector part $r_q \in \mathbb{R}^3$. For a vector $x \in \mathbb{R}^3$, with transpose $x^\intercal$, we denote by $\bar{x}$ the quaternion with zero real part and vector part x, that is $\bar{x} = (0; x)$. The Hamiltonian quaternion product is given by $\otimes$, the vector cross product is denoted $\times$, and for a vector $x \in \mathbb{R}^3$ we define the skew-symmetric matrix

$$
S(x) = \begin{pmatrix} 0 & -x_3 & x_2 \\ x_3 & 0 & -x_1 \\ -x_2 & x_1 & 0 \end{pmatrix},
$$

with $x = (x_1; x_2; x_3)$. A block diagonal matrix M is indicated with $M = \mathrm{blockdiag}\,(M_1, M_2, \ldots, M_n)$ for some square matrices $M_1, M_2, \ldots, M_n$. The Moore-Penrose pseudo inverse is denoted $\dagger$. The sinc function is defined as

$$
\mathrm{sinc}(\alpha) := \begin{cases} 1 & \text{for } \alpha = 0 \\ \frac{\sin(\alpha)}{\alpha} & \text{otherwise,} \end{cases} \tag{1}
$$

for an angle α. Gaussian white noise n with mean μ and variance σ^2 is given as $n(\mu, \sigma^2)$.

Superscript indexes is used to indicate the coordinate system in which a given vector is decomposed, thus x^a and x^b refers to the same vector x decomposed in the coordinate systems indexed by a and b, respectively. The rotation between these coordinate systems may be represented by a quaternion q_a^b. The corresponding rotation matrix is denoted $R(q_a^b)$. The rate of rotation of the coordinate system indexed by b with respect to a, decomposed in c, is denoted ω_{ab}^c.

In the following, e denotes the Earth-Center-Earth-Fixed (ECEF) coordinate system, b for the vehicle BODY-fixed coordinate system, and i for the Earth-Centered Inertial (ECI) coordinate system.

Discretization and Measurements Samples

For the discrete-time implementation, the discretization interval T and a discrete time index k are utilized such that the continuous time variable t is related to T and k with $t = kT$ (for a constant T).

At a given index k all valid measurements at time $t = kT$ are contained in the measurements set $\mathcal{I}_k$ of measurements. If the i'th measurement is available and valid, this is indicated by $i \in \mathcal{I}_k$. The opposite case is denoted as $i \notin \mathcal{I}_k$.

Modeling

Kinematic Model

The rigid body kinematic model follows from [16] and [28],

$$\dot{p}^e = v^e, \tag{2}$$

$$\dot{v}^e = -2S(\omega_{ie}^e)v^e + f^e + g^e(p^e), \tag{3}$$

$$\dot{q}_b^e = \frac{1}{2}q_b^e \otimes \bar{\omega}_{ib}^b - \frac{1}{2}\bar{\omega}_{ie}^e \otimes q_b^e, \tag{4}$$

where p^e, v^e, $f^e \in \mathbb{R}^3$ are position, linear velocity and specific force in the ECEF frame, respectively.

The attitude of the vehicle is represented by a unit quaternion q_b^e. It represents the rotation from BODY to ECEF, and ω_{ib}^b represents the rotation rate of BODY with respect to ECI, while $\omega_{ie}^e = (0; 0; \omega_{ie})$, where ω_{ie} represents the Earth's rotation rate, which is assumed to be constant. Equivalently, by representing the attitude as a rotation matrix, (4) is realized as

$$\dot{R}_b^e = R_b^e S(\omega_{ib}^b) - S(\omega_{ie}^e)R_b^e. \tag{5}$$

The known vector $g^e(p^e)$ denotes the plumb-bob gravity vector, which is a function of the vehicle's position decomposed in the ECEF frame and is obtained with a gravity model.

Inertial and Magnetic Measurements

The inertial sensor model is chosen based upon strapdown technology, that is an IMU fixed to the BODY frame

$$f_{\text{IMU}}^b = f^b + \varepsilon_f^b, \tag{6}$$

$$\omega_{\text{IMU}}^b = \omega_{ib}^b + b_g^b + \varepsilon_\omega^b, \tag{7}$$

$$\dot{b}_g^b = \varepsilon_b^b, \tag{8}$$

where $f^b = R_e^b(a^e - g^e(p^e))$, with a^e being the acceleration relative the Earth measured by the IMU and where b_g^b denotes the gyro/angular rate bias. Accelerometer drift and biases are assumed to be compensated for using offline and online calibration methods such as [15, Sec. VI]. For details on IMUs, see "Inertial Measurement Units". Reference information about the heading may be obtained using a magnetometer that measures

$$m_{\text{mag}}^b = m^b + \varepsilon_m^b. \tag{9}$$

The variables ε_*^b represent measurement errors. Alternative sensors for providing heading information are compasses or GNSS-based heading obtained from multiple receiver measurements and a known baseline between the receivers.

With the kinematic vehicle model together with inertial and magnetic measurement models presented, the following section introduces the integration of GNSS and inertial measurements.

Nonlinear Observer for Integrated GNSS/INS Navigation
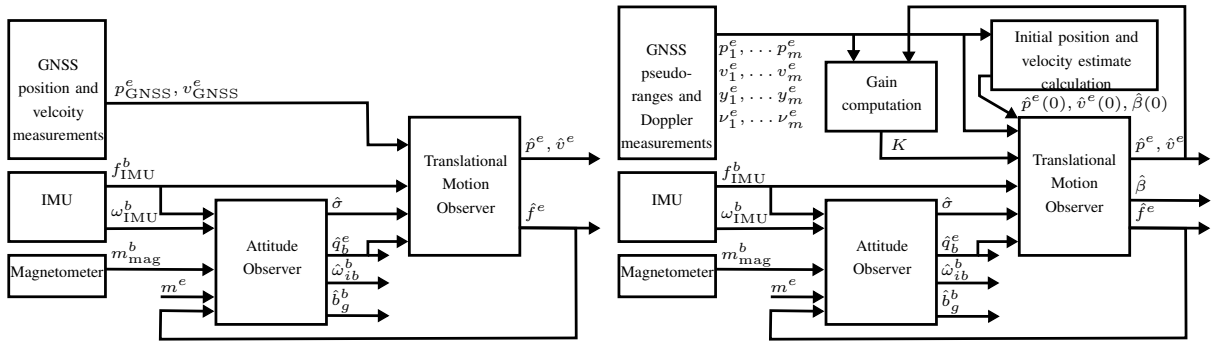
Overview

The two most common GNSS/INS integration techniques are known in the navigation literature as loosely coupled and tightly coupled integration, and are described below.

With loosely coupled integration the receiver's measurements of position, and sometimes velocity, are fused with the inertial measurements. When applying this integration strategy, the GNSS position and velocity measurements are given as $p_{\mathrm{GNSS}}^e = p^e + \delta_p$ and $v_{\mathrm{GNSS}}^e = v^e + \delta_v$ where δ_* represents the errors and noise. These are calculated by the receiver, in the ECEF frame, either with a Least Squares estimator or by using an EKF [5, Ch. 9.4].

With a tightly coupled integration strategy, the raw GNSS observables, pseudorange and Doppler range-rate, are utilized as aiding measurements by relating these to the inertial measurements using (2)–(4). In this article, the pseudorange and range-rate measurements are denoted y_i and ν_i, respectively, representing measurements from the i-th satellite out of m satellites in view. These measurements are determined based on the knowledge of satellite position and velocity, denoted p_i^e and v_i^e, calculated with the help of broadcasted satellite ephemeris. More details on GNSS are found in "GNSS – Position Calculation and Error Sources" and "GPS: The First GNSS – Signals and Positioning Services".

An advantage of the loosely coupled approach is the ease of implementation as the receiver takes care of all considerations about satellite constellation and integrity of the raw GNSS observables. On the other hand this also entails that only complete solutions can be used, whereas the tight integration approach can use a few raw GNSS observables that would be insufficient for a standalone solution. A disadvantage of tightly coupled integration is that not all receivers grants access to the raw GNSS observables, [5]. Moreover, the implementation and tuning of GNSS/INS integration is more straight forward with loosely coupled integration than with tightly coupled integration due to pseudorange measurements with different elevation angles may have considerably different noise characteristics. On the other hand, integrity monitoring is easier with tightly coupled integration in the range domain compared to its counterpart in the position domain since erroneous pseudorange measurements may be excluded while maintaining GNSS aiding. If a GNSS fault in loosely coupled integration is detected, GNSS aiding is lost until the fault has been remedied.

A schematic overview of the difference between the two integration strategies, applying
the same NLO for attitude determination, is shown in Fig. 3. Two key features are obtained using
the NLO in feedback interconnection with the TMO as depicted in Fig. 3; The first feature is
that the attitude is estimated without linearization, in opposite to KF-based techniques, making
the attitude observer robust to initialization errors allowing for large initial attitude errors. The
second, is that the attitude observer is utilizing the estimated specific force in the navigation
frame provided by the TMO as reference vector when calculating attitude corrections. The latter
feature is particularly useful when the navigation system is accelerated.

(a) Loosely coupled GNSS/INS integration

(b) Tightly coupled GNSS/INS integration. An algebraic pseudo-range solver is used to initialize the translational motion observer

Figure 3: Feedback-interconnected observer structures. An overview of the two feedback-interconnected observer structures used for integration of global navigation satellite systems (GNSS) and the inertial navigation system (INS) is presented. Fig. 3a shows the loosely coupled INS/GNSS integration. With loosely coupled integration there exists a standalone GNSS solution used as aiding for estimation of position and velocity. Fig. 3b shows the tightly coupled INS/GNSS integration. With this integration scheme, the position and velocity solution is obtained using GNSS pseudorange and Doppler range-rate measurements in combination with the inertial measurement unit (IMU) readings. With both integration techniques, the nonlinear attitude observer provides the translational motion observer (TMO) with the quaternion $\hat{q}_b^e$ and injection term $\hat{\sigma}$, while the TMO provides the attitude observer with the estimate of the specific force $\hat{f}^e$.

Attitude Observer

The proposed loosely and tightly coupled GNSS/INS integration schemes, are both dependent on the nonlinear attitude observer. The latter is presented in detail in this section,

where discretization prior to implementation, also is discussed.

The attitude observer used is based on [11] and [15], [16], employing complementary filtering,

$$\dot{\hat{q}}_b^e = \frac{1}{2}\hat{q}_b^e \otimes \left(\bar{\omega}_{\text{IMU}}^b - \bar{\hat{b}}_g^b + \bar{\hat{\sigma}}\right) - \frac{1}{2}\bar{\omega}_{ie}^e \otimes \hat{q}_b^e, \tag{10}$$

$$\dot{\hat{b}}_g^b = \text{Proj}\left(-k_I\hat{\sigma}, \|\hat{b}_g^b\|_2 \leq M_{\hat{b}}\right), \tag{11}$$

$$\hat{\sigma} = k_1 f_{\text{IMU}}^b \times R(\hat{q}_b^e)^\intercal \text{sat}_{M_f}(\hat{f}^e)$$
$$+ k_2 m_{\text{mag}}^b \times R(\hat{q}_b^e)^\intercal m^e, \tag{12}$$

where k_1, k_2, k_I are gains. k_I is the gain of the gyro/angular rate bias estimator, giving an integral effect in the NLO, whereas $\text{Proj}(\cdot)$ is a projection operator ensuring that the gyro/angular rate bias is bounded, $\|\hat{b}_g^b\|_2 \leq M_{\hat{b}}$. See [16] for details. The injection term $\hat{\sigma}$ is utilized to correct the attitude and compensate for the gyro bias in (10), by estimating it in (11), with the goal of obtaining an estimate of ω_{ib}^b with $\hat{\omega}_{ib}^b = \omega_{\text{IMU}}^b - \hat{b}_g^b$. The injection $\hat{\sigma}$ is based on comparing the measured vectors in the BODY frame, here specific force and magnetic field from the accelerometer and the magnetometer, respectively, with the corresponding reference vector in the ECEF frame, rotated to the BODY frame using $R(\hat{q}_b^e)$. If there are discrepancies between the two, the nonlinear injection term $\hat{\sigma}$ acts as an angular velocity in (10) to compensate for this error. The reference vectors in question are m^e, being the Earth's magnetic field and assumed to be known, and the estimated specific force $\hat{f}^e$. Moreover, $\text{sat}_{M_f}(\cdot)$ is a saturation operator, such that specific force estimate remains bounded, $\|\hat{f}^e\|_2 \leq M_f$. As in [16], $\hat{f}^e$ is obtained from the TMO, presented later on, which offers an accurate estimate $\hat{f}^e$ also when the vehicle is accelerated. This is beneficial, compared to assuming that $f^e \approx -g^e(\hat{p}^e)$, where the gravity component g^e is obtained with a gravity model based on the estimated position $\hat{p}^e$, an assumption that holds only when the vehicle in question is not exposed to acceleration for prolonged periods of time. More vector measurement/reference pairs may be added to (12) depending on the application. A minimum of two colinear vectors are required in order to guarantee convergence regardless of the vehicle trajectories. The injection term $\hat{\sigma}$ is calculated in a way that resembles how the linearized attitude error enters the measurement matrix when using the quaternion-based MEKF, [6], algorithm to estimate the attitude.

Alternative Implementation of the Injection Term and Continuous-time gain selection

There exist other alternatives than (12) to construct the vector measurement/reference pairs. Normalized versions of m^b_{mag}, m^e, f^b_{IMU} and $\mathrm{sat}_{M_f}(\hat{f}^e)$ can be implemented using

$$\underline{f}^b = \frac{f^b_{\mathrm{IMU}}}{\|f^b_{\mathrm{IMU}}\|}, \qquad \underline{m}^b = \frac{m^b_{\mathrm{mag}}}{\|m^b_{\mathrm{mag}}\|},$$

$$\underline{f}^e = \frac{\mathrm{sat}_{M_f}(\hat{f}^e)}{\|\mathrm{sat}_{M_f}(\hat{f}^e)\|}, \quad \underline{m}^e = \frac{m^e}{\|m^e\|}.$$

By doing so, the gains k_1 and k_2 can be viewed as cut-off frequencies of a complementary filter as described in [11], [19] with the same unit as the angular velocity ω^b_{IMU} in (12) since the vector pairs become dimensionless. This means that for motion with frequencies above k_1 (rad/s), the rate gyro is the primary sensor used for estimating the attitude in the directions excited by the first reference vector, while for lower frequencies, the first reference vector correction dominates. Similarly k_2 essentially determines the cut-off frequency for use of low-frequency information from the second reference vector. Furthermore, the construction of vector pairs may be additionally extended, inspired by the TRIAD algorithm [29], by crossing the k-th vector pair with the previous vector pair, making the vectors in each frame perpendicular to each other. Hence, the new vectors $\underline{v_1}^b$, $\underline{v_1}^e$, $\underline{v_2}^b$ and $\underline{v_2}^e$ take the form of,

$$\underline{v_1}^b = \underline{f}^b, \quad \underline{v_2}^b = \underline{f}^b \times \underline{m}^b,$$

$$\underline{v_1}^e = \underline{f}^e, \quad \underline{v_2}^e = \underline{f}^e \times \underline{m}^e,$$

resulting in $\hat{\sigma}$ becoming,

$$\hat{\sigma} = k_1 \underline{v_1}^b \times R(\hat{q}^e_b)^{\mathsf{T}} \underline{v_1}^e + k_2 \underline{v_2}^b \times R(\hat{q}^e_b)^{\mathsf{T}} \underline{v_2}^e, \tag{13}$$

with the possibility to increase the attitude estimation performance compared to using (12).

Alternatively, a linearization of the complementary attitude filter is provided in eq. (37) in [19], and may be used to develop an optimal gain selection algorithm given the noise covariances.

Discretization of the Attitude Observer

The rate gyro measurements are integrated at a high rate $f = 1/T$, updating the attitude estimates whenever a new angular rate measurement is available, as in [19]. If T is small enough to assume that $\hat{\omega}(t)$ remains constant between samples, the exact discretization of the kinematic equation (10), is obtained using

$$\hat{q}^e_b[k] = \mathrm{e}^{\left(\frac{T}{2}\Omega(\hat{\omega}[k])\right)} \mathrm{e}^{\left(-\frac{T}{2}\bar{\Omega}(\omega^e_{ie})\right)} \hat{q}^e_b[k-1], \tag{14}$$

where

$$\hat{\omega}[k] = \omega_{\text{IMU}}^b[k] - \hat{b}_g^b[k-1] + \hat{\sigma}[k],$$

$$\Omega(\omega) = \begin{pmatrix} 0 & -\omega^{\mathsf{T}} \\ \omega & -S(\omega) \end{pmatrix}, \quad \bar{\Omega}(\omega) = \begin{pmatrix} 0 & -\omega^{\mathsf{T}} \\ \omega & S(\omega) \end{pmatrix},$$

$$e^{\left(\frac{T}{2}\Omega(\omega)\right)} = \cos\left(\frac{T}{2}\|\omega\|_2\right) I_4$$

$$+ \frac{T}{2}\text{sinc}\left(\frac{T}{2}\|\omega\|_2\right) \Omega(\omega),$$

and

$$e^{\left(-\frac{T}{2}\bar{\Omega}(\omega)\right)} = \left(\cos\left(\frac{T}{2}\|\omega\|_2\right) I_4 \right.$$

$$\left. + \frac{T}{2}\text{sinc}\left(\frac{T}{2}\|\omega\|_2\right) \bar{\Omega}(\omega) \right)^{-1}.$$

According to [19], the expressions $\cos(\cdot)$ and $\text{sinc}(\cdot)$ can, in practice, be approximated for by their first- or second-order approximation or by using a lookup table to increase the computational efficiency of (14). After (14) is calculated, re-normalization of $\hat{q}_b^e$ is carried out to account for numerical round-off errors,

$$\hat{q}_b^e[k] = \frac{\hat{q}_b^e[k]}{\|\hat{q}_b^e[k]\|}. \tag{15}$$

The gyro bias estimate can be updated using exact integration of (11) as

$$\hat{b}_g^b[k] = \hat{b}_g^b[k-1] - T\, k_I[k]\, \hat{\sigma}[k], \tag{16}$$

where a projection algorithm, such as that of [15], is straightforward to add. In this implementation, one or both terms in $\hat{\sigma}[k]$ is not included if there is no valid vector measurement available at time index k. To ensure that the cut-off frequency, chosen for each measurement vector, maps from continuous to discrete time, $\hat{\sigma}[k]$ is implemented as

$$\hat{\sigma}[k] = \hat{\sigma}_1[k] + \hat{\sigma}_2[k], \tag{17}$$

such that if $i = 1 \in \mathcal{I}_k$, then $\hat{\sigma}_1[k]$ is implemented by

$$\hat{\sigma}_1[k] = \frac{\delta t_{\text{acc}}}{T} k_1[k]\, \underline{v_1}^b[k] \times R(\hat{q}_b^e[k-1])^{\mathsf{T}} \underline{v_1}^e[k], \tag{18}$$

else $\hat{\sigma}_1[k] = 0_{3\times1}$. If $i = 2 \in \mathcal{I}_k$, then

$$\hat{\sigma}_2[k] = \frac{\delta t_{\text{mag}}}{T} k_2[k]\, \underline{v_2}^b[k] \times R(\hat{q}_b^e[k-1])^{\mathsf{T}} \underline{v_2}^e[k], \tag{19}$$

else $\hat{\sigma}_2[k] = 0_{3\times1}$. δt_{acc} and δt_{mag} denote the time intervals since the previous valid accelerometer and magnetometer measurements were available, respectively. This ensures that gains and

13

bandwidth of the respective vector measurements are independent of sampling frequency and only decided by the continuous-time cut-off frequencies k_1 and k_2. Typically, the specific force measurement is available at the same rate as the rate gyro readings such that $\delta t_{\mathrm{acc}} = T$. In this case

$$\hat{\sigma}_1[k] = k_1[k]\,\underline{v_1}^b[k] \times R(\hat{q}_b^e[k-1])^\mathsf{T}\underline{v_1}^e[k],$$

if $i = 1 \in \mathcal{I}_k$. This implementation strategy assumes that a valid specific force measurement

2 is available when a new magnetometer measurement is available due to the cross product of normalized vectors embedded in the implementation of $\hat{\sigma}_2[k]$. An outline of the implementation

4 of the nonlinear attitude observer is presented in "Algorithm 1".

The described implementation strategy, for nonlinear and potentially low-rate injection

6 terms is in compliance with the corrector-predictor scheme presented in [20, Ch. 11.3.4] and allows for k_1, k_2 and k_I to be time-varying.

8 With the attitude estimator defined, the following two sections present the loosely and tightly coupled TMOs in detail.

Loosely Coupled Translation Motion Observer

10

The TMO presented first is used together with the attitude observer to perform the loosely

12 coupled GNSS/INS integration. In addition to the algorithm itself, conditions for stability, and gain selection are presented. Discretization and implementation considerations are also covered.

For loosely coupled GNSS/INS integration, the TMO is obtained from [16],

$$\dot{\hat{p}}^e = \hat{v}^e + \theta K_{pp}^0(p_{GNSS}^e - \hat{p}^e) \tag{20}$$
$$+ K_{vp}^0(v_{GNSS}^e - \hat{v}^e),$$

$$\dot{\hat{v}}^e = -2S(\omega_{ie}^e)\hat{v}^e + \hat{f}^e + g^e(\hat{p}^e)$$
$$+ \theta^2 K_{pv}^0(p_{GNSS}^e - \hat{p}^e) \tag{21}$$
$$+ \theta K_{vv}^0(v_{GNSS}^e - \hat{v}^e),$$

$$\dot{\xi} = -R(\hat{q}_b^e)S(\hat{\sigma})f_{\mathrm{IMU}}^b$$
$$+ \theta^3 K_{p\xi}^0(p_{GNSS}^e - \hat{p}^e) \tag{22}$$
$$+ \theta^2 K_{v\xi}^0(v_{GNSS}^e - \hat{v}^e),$$

$$\hat{f}^e = R(\hat{q}_b^e)f_{\mathrm{IMU}}^b + \xi. \tag{23}$$

14 The rotation matrix $R(\hat{q}_b^e)$ is obtained from the standard formula $R(\hat{q}_b^e) = I_3 + 2s_q S(r_q) + 2S^2(r_q)$. The state ξ is an auxiliary parameter/state, necessary to assist the estimation of the specific force

f^e, motivated by the analysis in [27] applied in [16], [17]. This state couples the rotational and translational motions, facilitating precise attitude estimation also when the vehicle is accelerated. The feedback of $\hat{f}^e$ from the TMO to the attitude observer requires stability analysis leading to some restrictions on the observer gains, that are discussed next.

Stability Conditions

The TMO for loosely coupled integration can now be written as a continuous-time linear system,

$$\dot{\hat{x}}^* = A^*\hat{x}^* + B^*u^* + D^*(t, \hat{x}^*) + K^*(y - C^*\hat{x}^*), \tag{24}$$

with the state, input and output, defined respectively as

$$\hat{x}^* := (\hat{p}^e; \hat{v}^e; \xi),$$
$$u^* := (f^b_{\text{IMU}}; -S(\hat{\sigma})f^b_{\text{IMU}}),$$
$$y := (p^e_{GNSS}; v^e_{GNSS}),$$

and with the matrices,

$$A^* = \begin{pmatrix} 0_{3\times3} & I_3 & 0_{3\times3} \\ 0_{3\times3} & 0_{3\times3} & I_3 \\ 0_{3\times3} & 0_{3\times3} & 0_{3\times3} \end{pmatrix},$$

$$B^* = \begin{pmatrix} 0_{3\times3} & 0_{3\times3} \\ R(\hat{q}^e_b) & 0_{3\times3} \\ 0_{3\times3} & R(\hat{q}^e_b) \end{pmatrix}, \quad D^*(t, \hat{x}^*) = \begin{pmatrix} 0_{3\times1} \\ g^e(\hat{p}^e) - 2(\omega^e_{ie})\hat{v}^e \\ 0_{3\times1} \end{pmatrix},$$

$$C^* = \begin{pmatrix} I_3 & 0_{3\times3} & 0_{3\times3} \\ 0_{3\times3} & I_3 & 0_{3\times3} \end{pmatrix},$$

$$K^* = \begin{pmatrix} K_{pp} & K_{vp} \\ K_{pv} & K_{vv} \\ K_{p\xi} & K_{v\xi} \end{pmatrix} = \begin{pmatrix} \theta K^0_{pp} & K^0_{vp} \\ \theta^2 K^0_{pv} & \theta K^0_{vv} \\ \theta^3 K^0_{p\xi} & \theta^2 K^0_{v\xi} \end{pmatrix},$$

such that the system (A^*, B^*, C^*) is both controllable and observable.

For the nominal case when there are no sensor errors or noise, the uniform semiglobal exponential stability (USGES) of the feedback interconnection of the attitude and translational motion observers is established in [16] under the following conditions:

- The two attitude reference vectors are not colinear. This is satisfied if there exists a constant $c_{\text{obs}} > 0$ such that $||m^e \times \hat{f}^e||_2 \geq c_{\text{obs}}$ or $||\underline{v_1}^e \times \underline{v_2}^e||_2 \geq c_{\text{obs}}$. Temporary violation of this

assumption can be tolerated since the attitude estimate can be updated using only the angular rate measurements for shorter periods of time.

- Attitude observer parameters satisfy $k_1, k_2 \geq k_P$ for some $k_P > 0$ and $k_I > 0$.
- The constant gains in the matrix

$$K^0 = \begin{pmatrix} K_{pp}^0 & K_{vp}^0 \\ K_{pv}^0 & K_{vv}^0 \\ K_{p\xi}^0 & K_{v\xi}^0 \end{pmatrix},$$

of the TMO can be chosen arbitrarily provided that the linear error dynamics matrix $A^* - K^0C^*$ is Hurwitz, and $\theta \geq \theta^*$, where $\theta^* \geq 1$ is sufficiently large, [16]. The intuitions behind a large θ is that it implies that the estimate of $\hat{f}^e$ is dominated by the GNSS measurement such that the attitude estimation errors do not lead to a large error in $\hat{f}^e$, which could otherwise destabilize the attitude observer.

The practical implication of the USGES stability properties is the robustness to arbitrarily large initialization errors in both position and attitude since no linearization is needed in the nonlinear attitude estimator.

Continuous-time Gain Selection

The gain conditions of [16], reviewed above, are of limited practical use since they are general and sufficient (not always necessary) conditions where a non-conservative bound θ^* may be difficult to find. Moreover, θ^* also depends on the attitude observer gains k_1, k_2, k_I. In a practical approach to tuning, the gains in the matrix K_0 of the TMO may be tuned using a minimum-variance estimation criterion by taking into account the influences of noises on its measurements. This is done by choosing $\theta = 1$ and

$$Q^* = \text{blockdiag}(S_f, S_{\hat{\sigma}f}), \qquad\qquad R = \text{blockdiag}(S_p, S_v),$$

as input and output noise covariance matrices, respectively. Regarding R, the matrices S_p and S_v represents the covariance matrices of the position and velocity measurement noise components ε_p and ε_v, respectively. In practice the GNSS position and velocity measurements are time-varying and correlated as the user position estimates are used to determine the user-to-satellite line-of-sight (LOS) vector in the velocity computation procedure. An alternative can then be to include cross terms S_{pv} and S_{vp} such that

$$R = \begin{pmatrix} S_p & S_{pv} \\ S_{vp} & S_v \end{pmatrix}, \quad S_{pv} = S_{vp}.$$

The covariance matrices S_f and $S_{\hat{\sigma}f}$ are obtained from the accelerometer's measurement noise by $S_f = E[\varepsilon_f \varepsilon_f^\mathsf{T}]$ and $S_{\hat{\sigma}f} = E[S(\hat{\sigma})\varepsilon_f \varepsilon_f^\mathsf{T} S^\mathsf{T}(\hat{\sigma})]$. The latter term goes to a steady-state value when the attitude estimates has converged.

16

A gain matrix that gives an approximately minimum variance estimate is given by the Riccati equation solution $P^* = (P^*)^\intercal > 0$ motivated by the fact that the TMO's error dynamics are identical to the time-scaled error dynamics of the Kalman-Bucy filter [30]

$$K^0 = P^*(C^*)^\intercal R^{-1}, \tag{25}$$

$$\frac{1}{\theta}\dot{P}^* = A^*P^* + P^*(A^*)^\intercal + B^*Q^*(B^*)^\intercal \\ - P^*(C^*)^\intercal R^{-1}C^*P^*. \tag{26}$$

One reason for (24)–(26) only being an approximately minimum variance estimator is that $\hat{q}_b^e$ and $\hat{\sigma}$ are correlated with f_{IMU}^b. Therefore the accelerometer's noise ε_f and the accompanying covariance S_f are correlated with B^*. The result of [26, Lemma 6] shows that it is possible to choose θ independently from P^*, using the time-varying Riccati equation (26) such that the USGES stability properties posed in [16] still hold when calculating the gains with (25)–(26). However, choosing $\theta > 1$ is suboptimal with respect to the minimum variance optimization problem the Kalman-Bucy filter solves. In addition, the covariance matrix $S_{\hat{\sigma}f}$, associated with ξ, is not necessarily straight forward to determine since $S(\hat{\sigma})$ is correlated with ε_f^b. These terms are also further correlated with $R(\hat{q}_b^e)$. As an alternative, ad hoc tuning of $S_{\hat{\sigma}f}$ can be considered. By always choosing $S_{\hat{\sigma}f}$ larger than zero, the gains associated with the state ξ never become zero, guaranteeing stability.

The TMO realization presented above can be referred to as a *direct filter* or *total state* implementation in the navigation literature, [3, Ch. 7.4]. In practice, this means that the filter's Riccati equation (26) is implemented at the frequency of the IMU and that the aiding sensors are used to correct the INS when available. As a result, for high integration frequencies, the computational burden might be considerable. Therefore, more computationally efficient alternatives are desirable, while still maintaining time-varying gains. This is possible to achieve since the time-varying dynamics of (26) is slowly-varying.

Example

To study the effects of the gain synthesis suggested for the feedback-interconnected observer above, inertial sensors and position measurements with white Gaussian noise are simulated, and both fixed and time-varying gain schemes are applied to the observers. This is a simplification, made for illustrative purposes, since in general both position and inertial sensors provide measurements containing noise with colored spectral content. The results are transformed to North-East-Down (NED) coordinates. Conversion from ECEF to NED coordinates is performed by first acquiring the estimated latitude $\hat{\mu}$ and longitude $\hat{l}$ from the position estimate $\hat{p}^e$ for instance in closed form with [31]. This information is then used to rotate the ECEF estimates

17

to NED with the quaternion $\hat{q}_n^e = \hat{q}_\mu \otimes \hat{q}_l$, where $\hat{q}_\mu = (\cos((\hat{\mu} + \pi/2)/2), 0, \sin((\hat{\mu} + \pi/2)/2), 0)^\mathsf{T}$ and $\hat{q}_l = \left(\cos(\hat{l}/2), 0, 0, -\sin(\hat{l}/2) \right)^\mathsf{T}$.

The respective transient performance is shown in Figs. 4–6 implemented with IMU noise characteristics $\varepsilon_\omega \sim n(0, 0.0025^2)$ and $\varepsilon_f \sim n(0, 0.05^2)$ using position as the only aiding TMO measurement. The GNSS noise characteristics where realized using $\varepsilon_p \sim (\varepsilon_{p_n}; \varepsilon_{p_e}; \varepsilon_{p_d})$ with $\varepsilon_{p_n} \sim n(0, 1.1^2)$, $\varepsilon_{p_e} \sim n(0, 1.1^2)$, and $\varepsilon_{p_d} \sim n(0, (1.5 \cdot 1.1)^2)$ such that the GNSS is less accurate in the vertical component after converting to NED.

The fixed-gain synthesis is done with $\theta = 1$ and the algebraic Riccati equation,

$$
\begin{aligned}
& A^* P^* + P^* (A^*)^\mathsf{T} + B^* Q^* (B^*)^\mathsf{T} \\
& - P^* (C^*)^\mathsf{T} R^{-1} C^* P^* = 0.
\end{aligned}
\tag{27}
$$

For both observers, the TMOs were synthesized using $S_f = 0.05^2 \cdot I_3$, $S_{\hat{\sigma} f} = 0.5 \cdot 0.05^2 \cdot I_3$ and $S_p = \text{blockdiag}(1.1 \cdot I_2, 1.65^2)$, after converting from ECEF to NED coordinates, with initial NED position and attitude error of $\tilde{p}(0) = (10, -7, 4)^\mathsf{T}$ m and $\tilde{\phi}(0) = 10$, $\tilde{\theta}(0) = 7$, $\tilde{\psi}(0) = -10$ degrees, respectively. The attitude gains where chosen as $k_1 = k_2 = 0.5$, $k_I = 0.01$. In the time-varying filter implementation the initial covariance $P(0)$ was chosen as $P(0) = \text{blockdiag}(10^2 \cdot I_3, I_3, I_3)$. A third case was also run with higher attitude gains $k_1 = k_2 = 20$ during the first 100 seconds, together with the time-varying TMO solution. The transient performance obtained is based on simulated sensors at rest.

The transient performance of the position, velocity and attitude errors is improved using the time-varying Kalman filter to synthesize the TMO as seen in Figs. 4–6. As indicated, in Fig. 6 by improving the TMO's estimates, improvements in the attitude convergence properties are also obtained. The fastest attitude covariance properties are witnessed with both a time-varying TMO and higher prescribed initial attitude gains as seen in Fig. 6. What also can be seen from Figs. 4–5, is that the convergence properties of the position and velocity estimates are not improved by time-varying attitude gains. It can also been seen in Figs. 4–6 that the estimates have to fully converged at 100 seconds. This is due to the gyro bias estimates have not yet fully converged to the true gyro biases.

Position Space GNSS Error Models

The position and velocity measurements provided by the GNSS receiver's least squares estimator or EKF are subjected to time-varying errors inflicted by three main effects; Satellite errors, signal propagation errors and receiver errors [4, Ch. 7], as presented in "GNSS – Position Calculation and Error Sources".
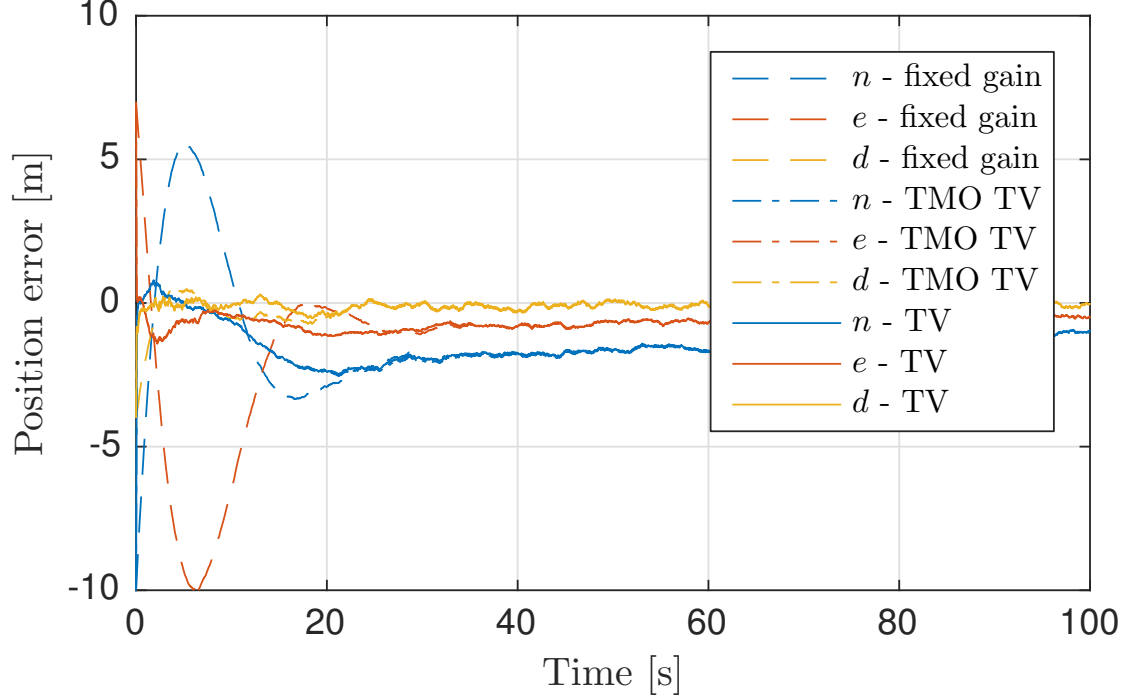
18

Figure 4: Position estimation error. The position errors obtained with the steady-state Kalman gain are presented with dash lines. The position errors obtained with the translational motion observer (TMO) applying a time-varying Kalman gain are shown using dash-dot lines. The error in position obtained when both the TMO and the attitude observer applied time-varying gains is shown using solid lines. The results indicate that using a TMO with time-varying gains toghter with an attitude observer prescribed with high initial gains accelerates the convergence of the position estimates to the true position.

The GNSS position and velocity errors can be characterized by their spectral contents. Using spectral factorization and a state-space realization of the resulting filtered white noise processes for loosely coupled integration leads to an m-th order linear error model on the form

$$\dot{z} = Fz + Gn, \qquad \delta = Hz + \varepsilon_{pv}, \tag{28}$$

where $\delta = (\delta_p; \delta_v) \in \mathbb{R}^6$ represents the position and velocity errors, and $\varepsilon_{pv}^e \in \mathbb{R}^6$ and $n \in \mathbb{R}^6$ are vectors with unity white noise where $n \sim (0, 1)$ and $\varepsilon_{pv}^e \sim (0, \sigma_{pv}^2)$. Hence, the receiver outputs position and velocity estimates $p_{\text{GNSS}}^e = p^e + \delta_p$ and $v_{\text{GNSS}}^e = v^e + \delta_v$, respectively. The model (28), related to the GNSS position measurements can be chosen to be a first-order Gauss-Markov process [32], [33]. By defining $z := (z_p; z_v)$, the dynamic GNSS position error is represented by the system

$$\dot{z}_p = F_p z_p + G_p n_p, \qquad \delta_p = H_p z_p + \varepsilon_p, \tag{29}$$
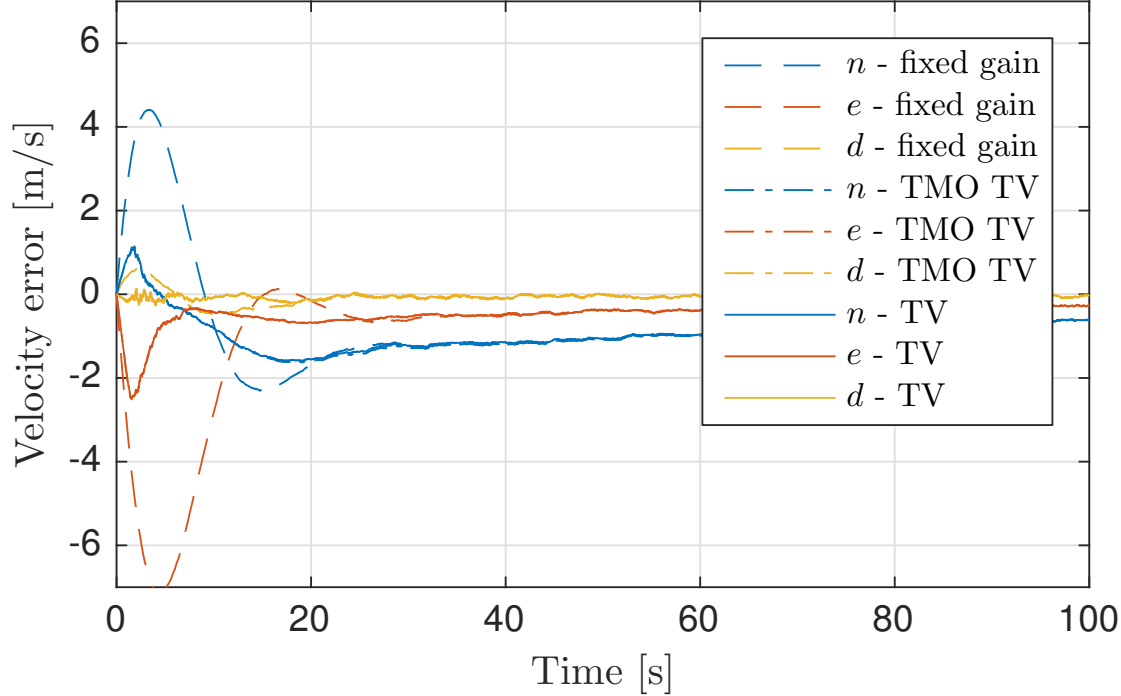
19

Figure 5: Velocity estimation error. The velocity errors obtained with the steady-state Kalman gain are presented with dash lines. The velocity errors obtained with the translational motion observer (TMO) applying a time-varying Kalman gain are shown using dash-dot lines. The error in velocity obtained when both the TMO and the attitude observer applied time-varying gains is shown using solid lines. The results indicate that using a TMO with time-varying gains, with or without an attitude observer prescribed with high initial gains, accelerates the convergence of the velocity estimates to the true velocity compared to the fixed-gain solution.

with $F_p = -T_p^{-1}$, where T_p is the correlation time constant. G_p is chosen equal to the appropriate standard deviation of the driving noise.

It is evident that even though the GNSS velocity measurements can be very precise (RMS error of down to 0.1 m/s), these also contain some dynamic errors, depending on satellite geometry and the resulting effects on measurement precision. See "GPS: The First GNSS – Signals and Positioning Services". Moreover, for the dynamic error of the GNSS velocity measurement can be represented by

$$\dot{z}_v = F_v z_v + G_v n_v, \qquad \delta_v = H_v z_v + \varepsilon_v. \tag{30}$$

By choosing $F_v = -T_v^{-1}$ where T_v is the assumed correlation time and G_v corresponding to the standard deviation of the driving noise (30), the steady-state covariance of the Gauss-Markov
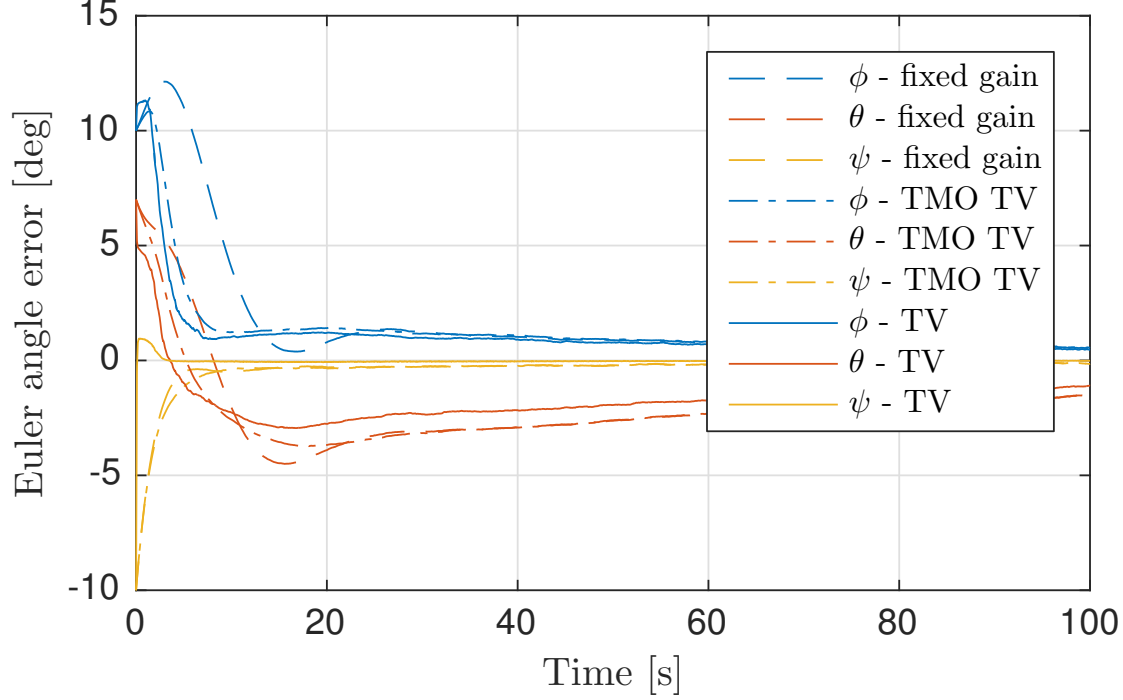
Figure 6: Attitude estimation error. The attitude error is presented applying Euler angles as attitude representation. The attitude errors obtained in feedback interconnection with the translational motion observer (TMO) using a steady-state Kalman gain are presented with dash lines. The attitude errors obtained in connection with the TMO applying a time-varying Kalman gain are shown using dash-dot lines. The attitude error obtained when both the TMO and the attitude observer applied time-varying gains is shown using solid lines. The results indicate that using a TMO with time-varying gains in feedback interconnection with an attitude observer prescribed with high initial gains accelerates the convergence of the attitude estimates to the true attitude.

processes z_p and z_v become

$$P_{z_p}(\infty) = -\frac{1}{2}F_p^{-1}G_pG_p^\mathsf{T}, \quad P_{z_v}(\infty) = -\frac{1}{2}F_v^{-1}G_vG_v^\mathsf{T}, \tag{31}$$

respectively for sufficiently long measurement periods since $F_p = F_p^\mathsf{T}$, $F_v = F_v^\mathsf{T}$. For higher-order models $P_{z_\star}(\infty)$ is obtained by solving

$$F_\star P_{z_\star} + P_{z_\star}F_\star^\mathsf{T} + G_\star G_\star^\mathsf{T} = 0_{l\times l}, \tag{32}$$

where $\star$ is a placeholder for p or v and l being the dimension of $F_\star$.

Augmented TMO for Loosely Coupled Integration Including GNSS Error Models

To account for colored GNSS measurement noise, the TMO is augmented with an estimator of the noise dynamics

$$\dot{\hat{z}} = F\hat{z} + K_{pz}(p^e_{GNSS} - \hat{p}^e - \hat{\delta}_p)$$
$$+ K_{vz}(v^e_{GNSS} - \hat{v}^e - \hat{\delta}_v), \tag{33}$$

such that the augmented state vector becomes $x = (x^*; z)$ which is leads to

$$\dot{x} = Ax + B_1 u^* + B_2 n + D, \tag{34}$$

and the corresponding TMO

$$\dot{\hat{x}} = A\hat{x} + B_1 u^* + D(t, \hat{x}) + K(y - C\hat{x}), \tag{35}$$

where the augmented system is defined by

$$A = \begin{pmatrix} A^* & 0_{9\times l} \\ 0_{m\times 9} & F \end{pmatrix}, \qquad C = \begin{pmatrix} C^*, & H \end{pmatrix},$$

$$B_1 = \begin{pmatrix} B^* \\ 0_{l\times 6} \end{pmatrix}, \qquad B_2 = \begin{pmatrix} 0_{9\times l} \\ G \end{pmatrix},$$

$$B = \begin{pmatrix} B_1 & B_2 \end{pmatrix}, \qquad D(t, \hat{x}) = \begin{pmatrix} D^*(t, \hat{x}) \\ 0_{l\times 1} \end{pmatrix},$$

$$K = \begin{pmatrix} K^* \\ K_z \end{pmatrix},$$

and where B is used to calculate $K = \theta L_\theta^{-1} K^0 E_\theta$ from the augmented equivalent of (25)–(26), that is

$$K^0 = PC^{\mathsf{T}}R^{-1}, \tag{36}$$

$$\frac{1}{\theta}\dot{P} = AP + PA^{\mathsf{T}} + BQB^{\mathsf{T}}$$
$$- PC^{\mathsf{T}}R^{-1}CP, \tag{37}$$

with

$$L_\theta = \text{blockdiag}\left(I_3, \frac{1}{\theta}I_3, \frac{1}{\theta^2}I_3, I_{l_p}, \frac{1}{\theta}I_{l_v}\right), \tag{38}$$

$$E_\theta = CL_\theta C^{\dagger}. \tag{39}$$

Moreover, l is the degrees of freedom of the Gauss-Markov process and the dimension of G relating the driving noise n to the augmented state z. l_p and l_v are the respective dimensions of the GNSS position and velocity error models. If only the position measurement is corrupted

22

by colored noise, $l := 3$ resulting in $L_\theta = \text{blockdiag}\,(I_3, 1/\theta \cdot I_3, 1/\theta^2 \cdot I_3, I_l)$. However, if this is also applicable for the velocity measurement, $l := 6$ with the spectral factorization chosen above. The pair (A, C) can be shown to always be observable for any $T_p, T_v > 0$ when the chosen spectral factorization results in a first-order Gauss-Markov process since

$$\text{rank}(\mathcal{O}) = 9 + l, \tag{40}$$

where

$$\mathcal{O} = \left(C; CA; \ldots; CA^{9+l-1} \right), \tag{41}$$

hence satisfying Kalman's rank condition of observability of linear time-invariant systems, [30]. With this state-space augmentation, and by defining $Q = \text{blockdiag}\,(Q^*, I_l)$, the TMO is realized using (35) where the gain can be obtained using (36)–(37).

Example Continued: Effects of colored GNSS noise

GNSS position and velocity measurements contain colored noise components, as presented in "GNSS – Position Calculation and Error Sources" and "GPS: The First GNSS – Signals and Positioning Services". To illustrate the effect of the colored noise on the GNSS/INS integration performance, induced by (28), a GNSS receiver is simulated, at high latitude, where the measurement is given in the NED frame, $p^n_{\text{GNSS}} = p^n + z_p + \varepsilon_p$ and $v^n_{\text{GNSS}} = v^n + z_v + \varepsilon_v$ and the model parameters are chosen as $F = \text{blockdiag}(F_p, F_v)$ and $G = \text{blockdiag}(G_p, G_v)$ with

$$F_p = -1/T_p \cdot I_3, F_v = -1/T_v \cdot I_3,$$
$$G_p = \text{diag}(1.2, 0.7, 2),$$
$$G_v = \text{diag}(1, 1, 2).$$

The time constant of the position error was chosen to be $T_p = 1100$ s as in [32], [34, Ch 7.5], while the time constant for the velocity was chosen as $T_v = 2$ s. The latter was chosen based on the assumption that the GNSS velocity measurements, obtained from the receiver, primarily are based on the Doppler range-rate measurements. The time constant related to these can be much smaller than for the noise embedded in the C/A code-based pseudoranges. This is due to the GNSS carrier phase and code observables being affected differently by various error sources. Furthermore, with this choice of G, it is taken into account that the horizontal measurements are more accurate than the vertical counterparts and that the eastern measurements are more precise than the northern at higher latitudes using GPS. The chosen noise and bias parameters related to the simulated inertial sensors are equal to those presented in the previous simulation example.

The motion simulated is of a small UAV flying in a circular motion with a speed 25 m/s and with a constant altitude of 150 meters over ground. The UAV is flying with a constant

yaw rate with a roll angle and pitch angles of $\phi = -3$ and $\theta = 2$ degrees, respectively. The North-East motion in shown in Fig. 7.
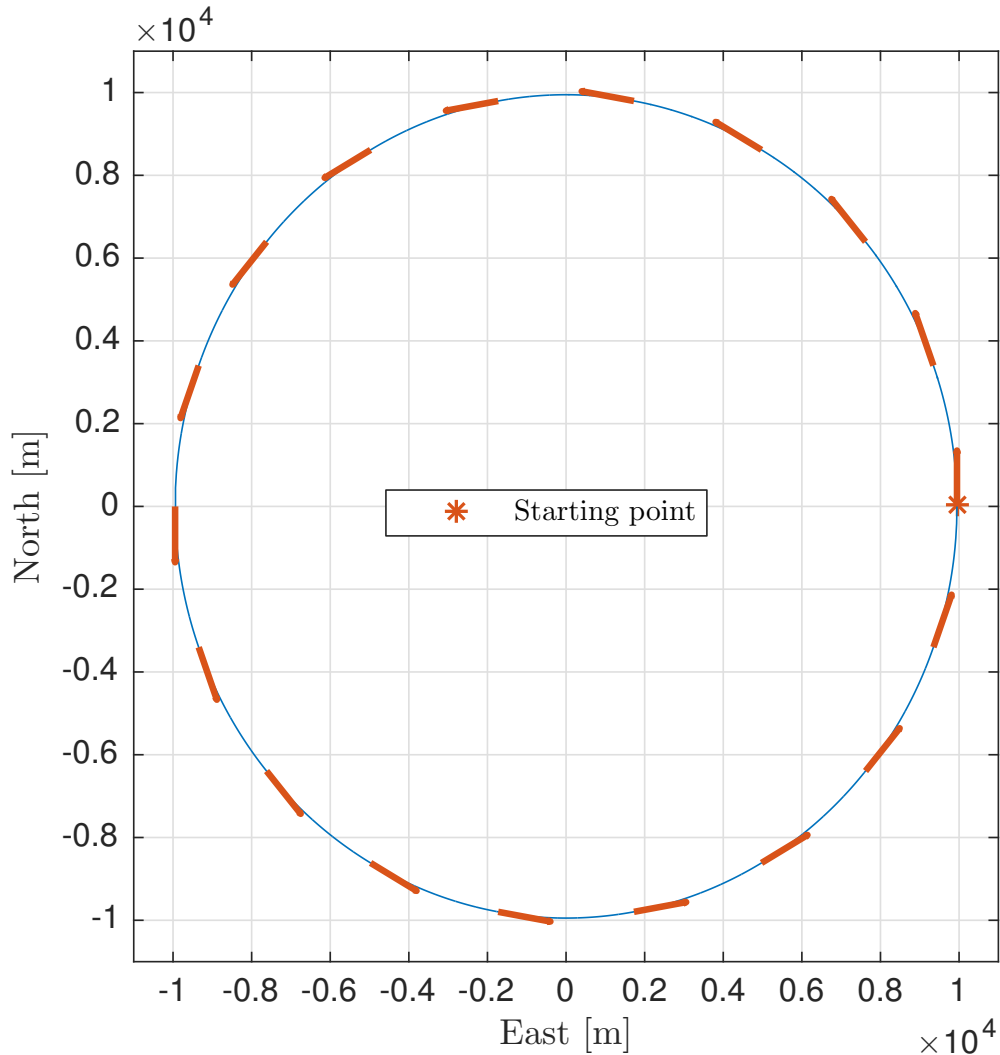

Figure 7: Overview of the simulated horizontal unmanned aerial vehicle (UAV) motion. The motion simulated is a circle with radius of 10 000 meters, where the initial heading of the UAV was zero. The chosen simulated UAV speed was 25 m/s. The blue circle indicates the UAV motion, while the red arrows depicts the heading of the UAV at fixed intervals.

Case 1: Only GNSS Position measurement available: This first case is simulated with only position measurements available.

Figs. 8–9 show the position estimation error and performance of the GNSS colored noise estimation. It is obvious that even though $\text{rank}\,(\mathcal{O}) = 12$, such that the pair (A, C) is observable,

the GNSS transient error is not captured by the model augmentation. Due to the stochastic
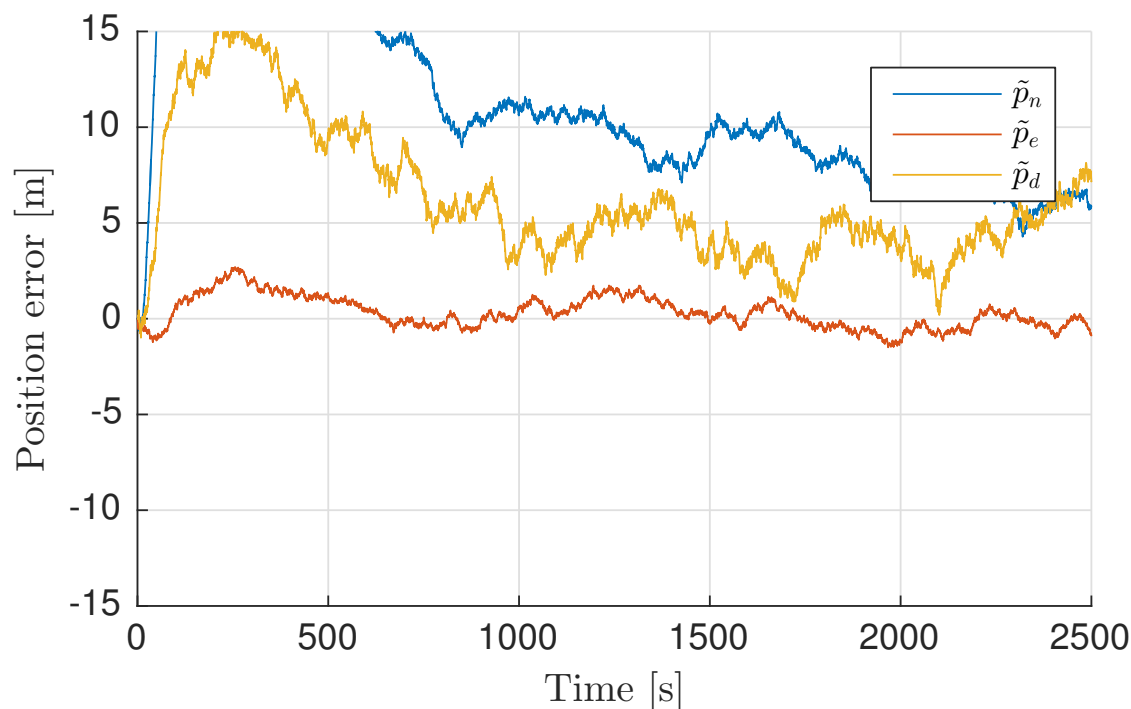

Figure 8: Case 1, position estimation error. The position estimation error obtained in simulation when applying global navigation satellite systems (GNSS) position measurements containing colored noise.

properties, in this case, the system (A, C) is only weakly observable as indicated by the estimation error covariance P. Fig. 10, based on the stationary estimation error covariance $P(\infty)$ shows the error ellipsis, with 95% confidence interval, illustrating that the states associated with the colored GNSS noise are highly correlated with the position error. Hence, it can be expected that the position covariance is close to that of (31), the Gauss-Markov process describing the colored noise.

Case 2: GNSS position measurements together and a velocity measurement with white noise: In this case, unrealistic GNSS velocity measurements are added, containing the true velocity and only corrupted with white noise for illustrative purposes.

Figs. 11–12 show the position estimation error and performance of the GNSS colored noise estimation error when the velocity measurements, only corrupted with white noise, are added as an aiding measurements in the TMO. The deterministic observability properties are still the same with rank 12, however the performance has increased significantly. Hence, now the TMO
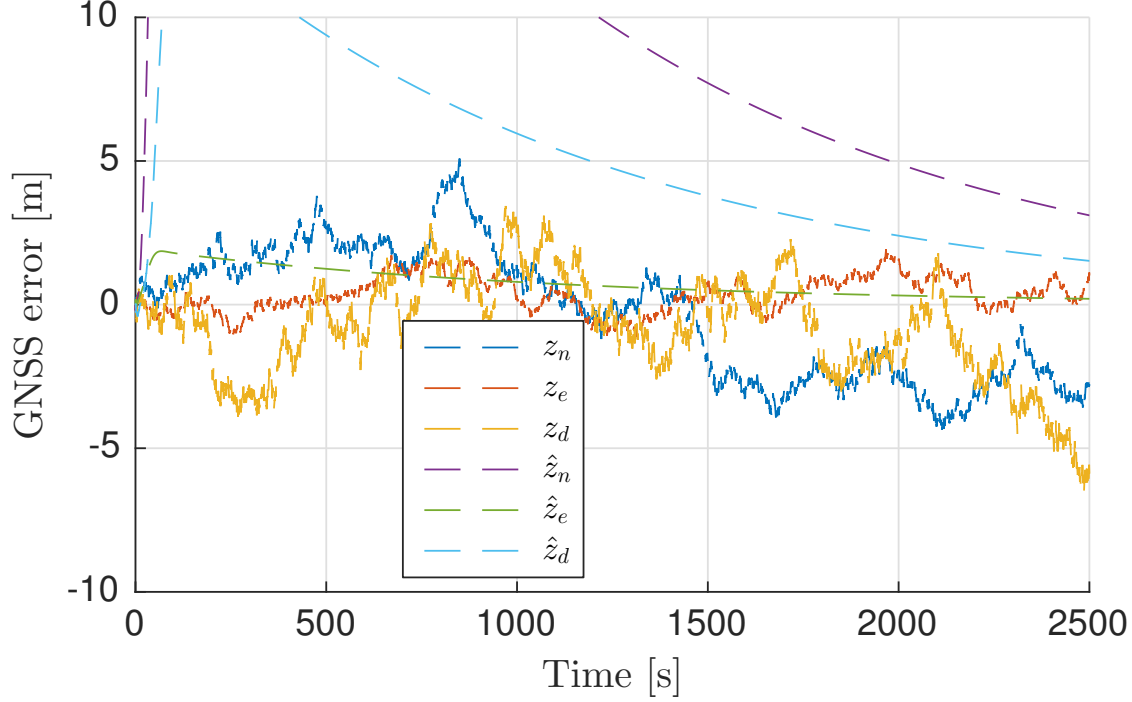
25

Figure 9: Case 1, global navigation satellite systems (GNSS) error state estimates. The true GNSS error states (colored noise) are shown in blue, red and yellow, respectively. The corresponding respective estimates are presented in purple, green and light blue. It can be seen that the translational motion observer fails in estimating the colored GNSS correctly.

is able to track the colored GNSS position error to a large extent. This is reflected in Fig. 11 where the position estimation error is reduced compared to the performance shown in Fig. 8.

Case 3: GNSS position and velocity measurements containing colored noise: In this last case, a more realistic GNSS velocity measurement is used, having some dynamic error such that $v_{\mathrm{GNSS}}^n = v^n + z_v + \varepsilon_v$, as described earlier, where z_v is generated as a Gauss-Markov process with time constant $T_v = 2$. Related to case 2 only minor differences are seen considering Figs. 13–14 compared to Figs. 11–12. The augmented observer structure of (35) is able to utilize the velocity measurements with colored noise, hence improving the position accuracy compared to Case 1 and Figs. 8–9. Even though the absolute position error is reduced compared to Case 1, the covariance of the estimation error still indicates the same problem; the TMO may still struggle to distinguish the colored noise of the position measurements from the true position as seen in Fig. 15 showing the error ellipse of $P(\infty)$, where the cross correlation between the $\tilde{p}$ and $\tilde{z}_p$ still is significant, however reduced compared to case 1 where only the position measurements were used.
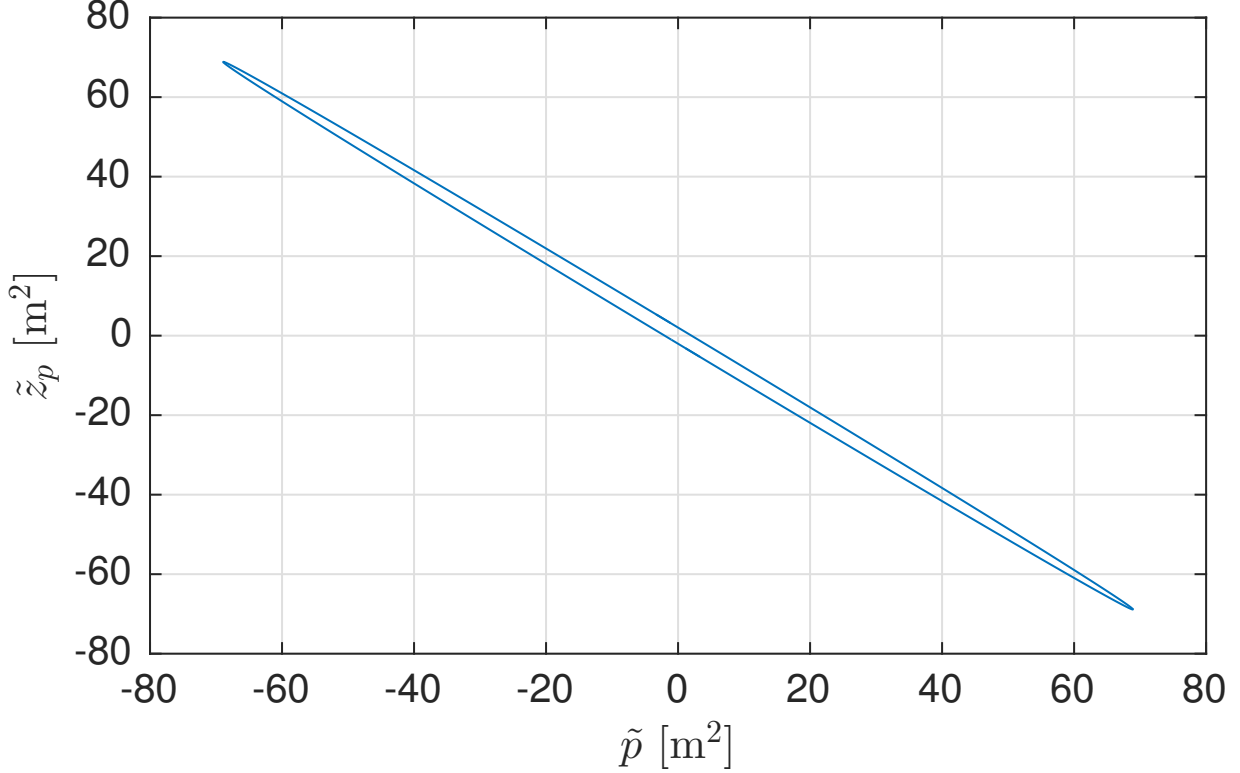
Figure 10: Case 1, error ellipsis of the north position estimation error and the corresponding colored noise estimate of the position measurement. The error ellipsis presented shows that the position estimation error and the colored GNSS noise estimation error are significantly correlated. This indicate that the translational motion observer struggles to separate the colored noise from the true position. Similar ellipsis are also obtainable for the East and Down axes.

Discussion:

The reason why the augmented observer, applying loosely coupled GNSS/INS integration, (35), struggles to separate the true position from the slowly-varying colored GNSS noise is the relatively high noise in the IMUs accelerometers. Since the rotated accelerometer noise is integrated twice in the TMO, the TMO gains are synthesized, using (36)–(37), such that the uncertainty in the position estimate is minimized and by that stabilizing the observer. Hence, the gains, in practice, become so large that the position estimate in the observer tracks the slowly-varying colored GNSS noise. To illustrate this, a Bode diagram, related to the northern position estimation error and the GNSS errors from Case 1 is shown in Fig. 16. The transfer functions shown, are the IMU noise ε_f^n rotated to the NED frame, to the position estimation error $\tilde{p} = p^n - \hat{p}^n$, the transfer function from the GNSS measurement error $\delta_p = H_p z_p + \varepsilon_p$ to the position estimation error, and the transfer function from the input of the GNSS colored noise
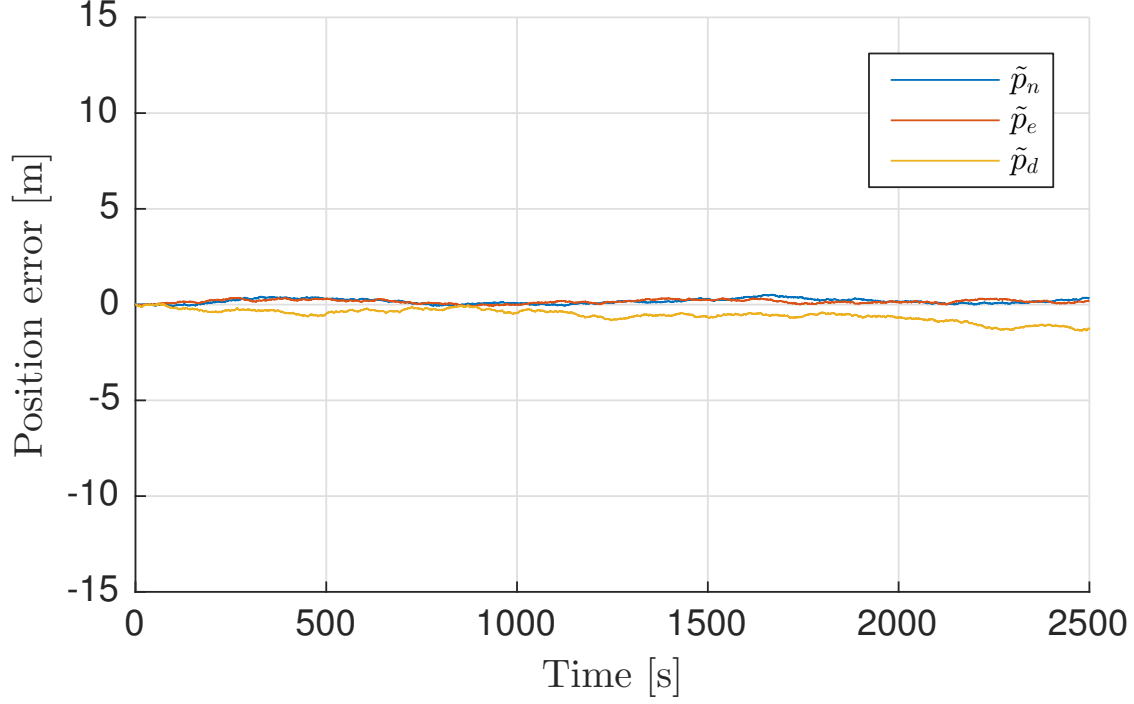
Figure 11: Case 2, position estimation error. The position estimation error obtained in simulation when applying global navigation satellite systems (GNSS) position measurements containing colored noise together with GNSS velocity measurements containing white noise. The estimation accuracy is better with velocity measurements corrupted by white noise compared to solely applying position measurements.

model n_p to the output of the model z_p. These are denoted

$$\frac{\tilde{p}}{\varepsilon_f^b} = h_{\text{INS}}(s), \tag{42}$$

$$h_{\text{INS}}(s) = \bar{C}\left(sI_3 - (A^* - K^*C^*)\right)^{-1} B^*, \tag{43}$$

and

$$\frac{\tilde{p}}{\delta_p} = h_{\text{PosErr}}(s), \tag{44}$$

$$h_{\text{PosErr}}(s) = \bar{C}\left(sI_3 - (A^* - K^*C^*)\right)^{-1} K^*C^*, \tag{45}$$

where $\bar{C} = (I_3,\, 0_{3\times3},\, 0_{3\times3})$ and

$$\frac{z_p}{n_p} = h_{\text{CN}}(s), \tag{46}$$

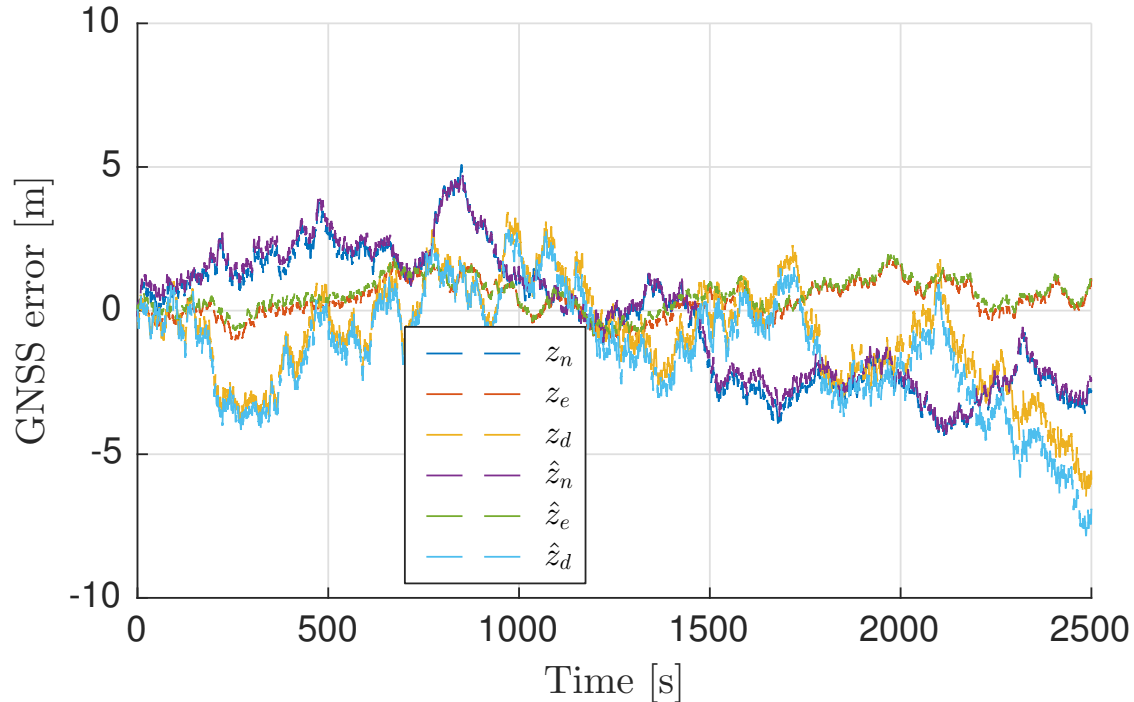$$h_{\text{CN}}(s) = I_3\left(sI_3 - (F_p)\right)^{-1} G_p, \tag{47}$$

28

Figure 12: Case 2, global navigation satellite systems (GNSS) error state estimates. The true GNSS error states (colored noise), associated with position, are shown in blue, red and yellow, respectively. The corresponding respective estimates are presented in purple, green and light blue. It can be seen that the translational motion observer estimates the colored GNSS error more accurate after the velocity measurements were introduced.

respectively. It is evident from Fig. 16 that the INS has higher bandwidth than the GNSS colored noise. This is due to the gains synthesis obtained from (36)–(37) is emphasizing the correction of the position estimate significantly more than the update of corresponding GNSS error state. As a result, the estimated position tracks the colored noise contained in the GNSS position measurements regardless of the model augmentation.

The results from Case 3 indicate that velocity measurements are beneficial to improve the position estimation accuracy, using loosely coupled GNSS/INS integration. However, the parameters representing the colored noise characteristics are time-varying and difficult to know in general. These are highly receiver dependent, and dependent on the user's location on Earth with respect to satellite geometry, elevation of the satellites, the ionosphere, and whether the Doppler observables are utilized in the GNSS's receiver estimator. In particular, knowledge on how the velocity measurements are calculated is difficult to know using off-the shelf equipment. Typically, the current position estimate is used in the velocity estimation process to determine user-to-
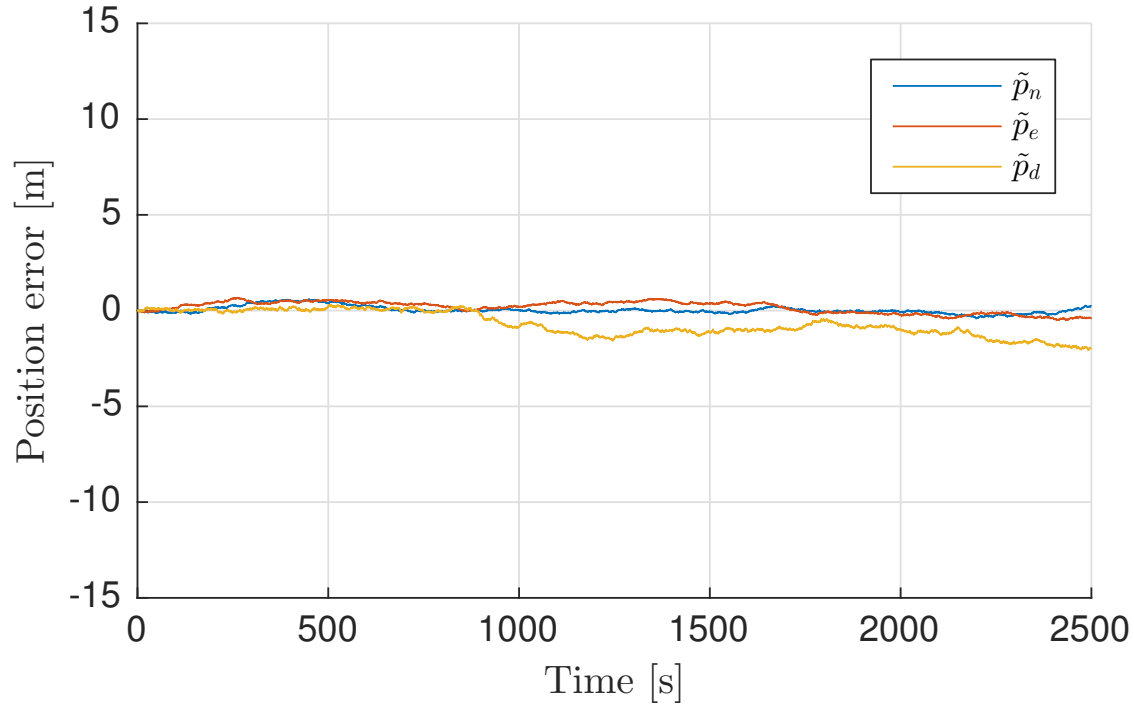
Figure 13: Case 3, position estimation error. The position estimation error obtained in simulation when applying global navigation satellite systems (GNSS) position and velocity measurements containing colored noise. The estimation accuracy is better with velocity measurements compared to solely applying position measurements, however, still worse than applying a velocity measurement only corrupted by white noise.

satellite LOS vectors or to estimate the receiver's velocity without the Doppler measurement, yielding that the position information is being accounted for twice in the GNSS/INS observer. Knowing the cross correlation between the position and velocity measurements are of utmost importance in such situations. If not known, using only the position measurements may be advised.

Discretization of TMO

The main principle for the discrete-time implementation is to approximate the continuous time behavior despite the finite data rate. It implies that the estimates are only updated when the output measurements contained in the injection terms are valid, and otherwise integrate the model using measured inputs at their highest available update rate. Measurement updates can be processed sequentially by a KF, assuming the measurements are uncorrelated such that the R matrix is diagonal, with benefits for processing structure and complexity [3], [5]. Due to the close
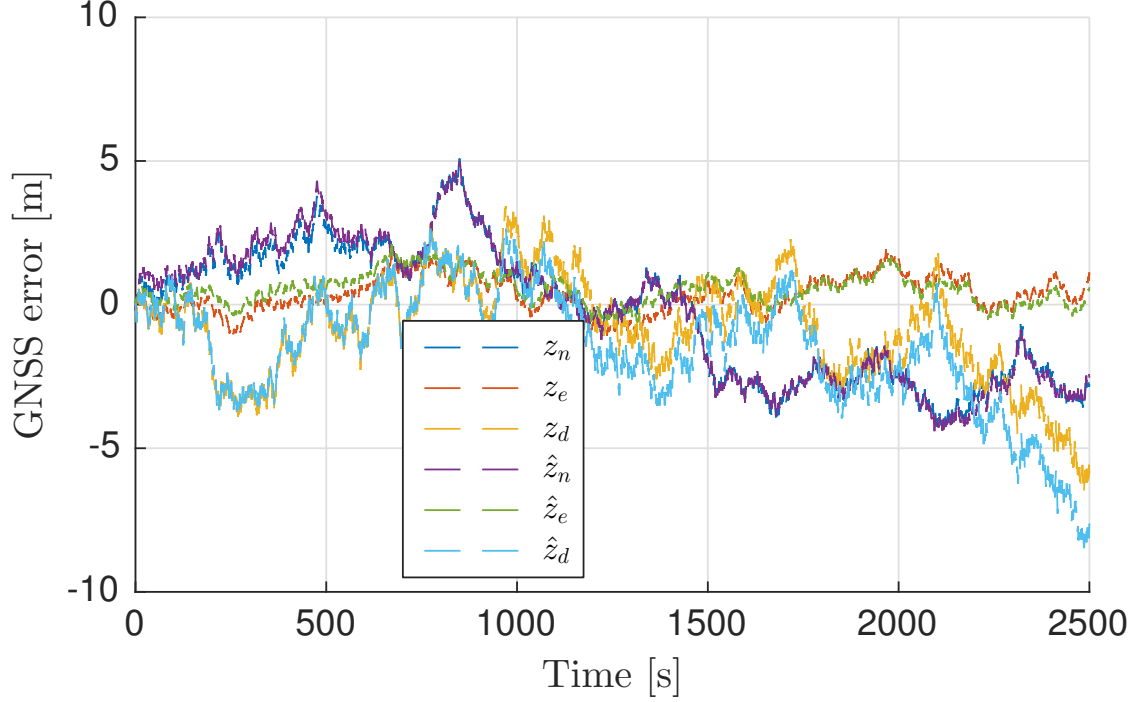
30

Figure 14: Case 3, global navigation satellite systems (GNSS) error state estimates. The true GNSS error states (colored noise), associated with position, are shown in blue, red and yellow, respectively. The corresponding respective estimates are presented in purple, green and light blue. It can be seen that the translational motion observer estimates the colored GNSS error more accurate with velocity measurements than without, however, not as accurate as when the velocity measurements only were corrupted with white noise.

relationship between (36)–(37) and the KF, a similar strategy can be applied also for NLOs. The TMO (35) is straightforward to discretize due to its linearity and the simple A-matrix, allowing for exact discretization of the unforced dynamics. In particular, the one-step ahead predicted state, x^- can be computed by

$$
\begin{aligned}
x^-[k+1] = {}& \mathrm{e}^{AT} x^+[k] \\
& + \int_{kT}^{(k+1)T} \mathrm{e}^{A\left((k+1)T-\tau\right)} B_1(\tau) u^*(\tau)\,\mathrm{d}\tau \\
& + \int_{kT}^{(k+1)T} \mathrm{e}^{A\left((k+1)T-\tau\right)} D(\tau)\mathrm{d}\tau,
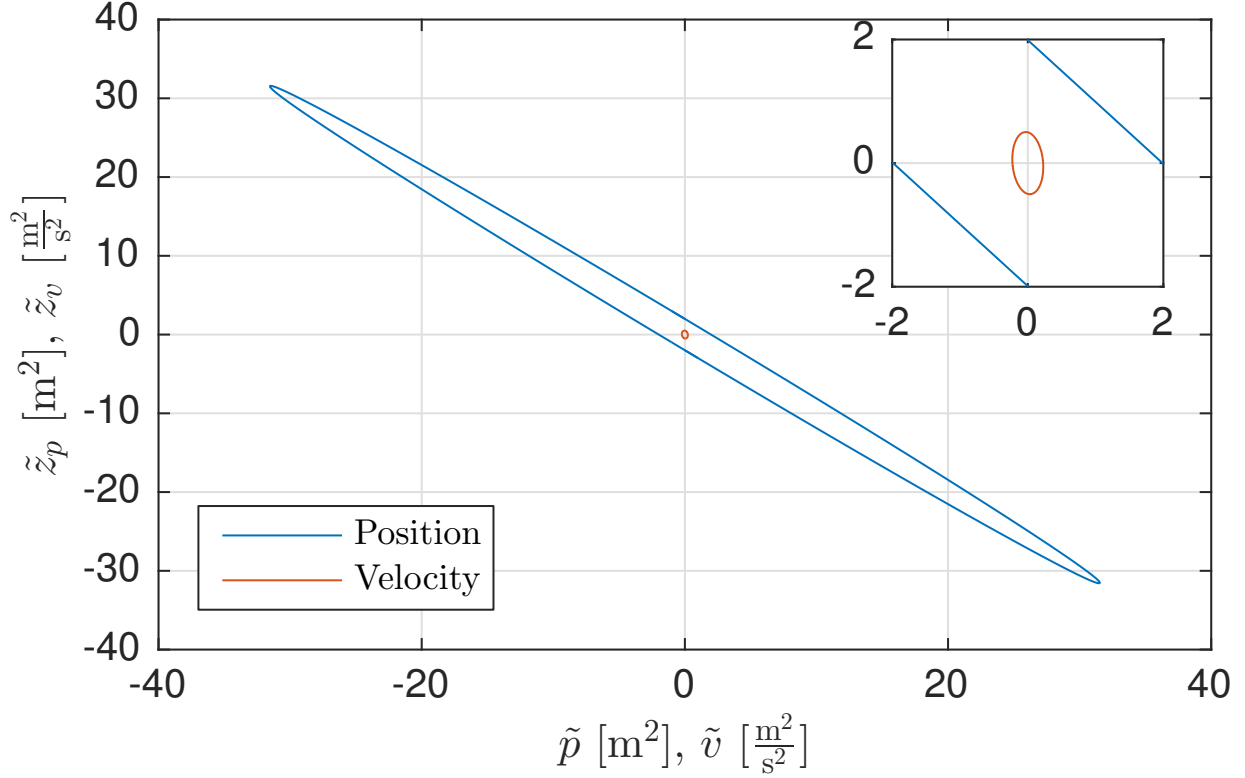\end{aligned}
\tag{48}
$$

31

Figure 15: Case 3, error ellipsis of the north position and velocity estimation error and the corresponding colored noise estimate of the position and velocity measurement. The error ellipsis associated with position is shown in blue, while error ellipsis associated the velocity is shown red. The error position ellipsis shows that the position estimation error and the colored global navigation satellite system noise estimation error still are significantly correlated, however, the correlation is significantly reduced by introducing the velocity measurement. Regarding the velocity estimation error and the velocity colored noise, the correlation is significantly smaller the compared to the position equivalent.

from the estimate $x^+[k]$, where

$$
A_d = \mathrm{e}^{AT} = \begin{pmatrix} I_3 & TI_3 & \frac{T^2}{2}I_3 & 0_{3\times l} \\ 0_{3\times 3} & I_3 & TI_3 & 0_{3\times l} \\ 0_{3\times 3} & 0_{3\times 3} & I_3 & 0_{3\times l} \\ 0_{l\times 3} & 0_{l\times 3} & 0_{l\times 3} & \mathrm{e}^{FT} \end{pmatrix}, \tag{49}
$$

based on the model parameters of (35). Assuming the specific force input, the rotation matrix and the gravity vector are constant between the sampling intervals, $f_{\mathrm{IMU}}^b(t) = f_{\mathrm{IMU}}^b[k]$, $R(t) =$

32

$R(q_b^e[k])$ and $g^e(p^e(t)) = g^e(\hat{p}^e[k])$, for $t \in [kT, (k+1)T)$, the definitions follows from (48)

$$B_{d,1}[k] := \begin{pmatrix} \frac{T^2}{2}R(\hat{q}_b^e[k]) & \frac{T^3}{6}R(\hat{q}_b^e[k]) \\ TR(\hat{q}_b^e[k]) & \frac{T^2}{2}R(\hat{q}_b^e[k]) \\ 0_{3\times3} & TR(\hat{q}_b^e[k]) \\ 0_{l\times3} & 0_{l\times3} \end{pmatrix},$$

$$B_{d,2}[k] := \begin{pmatrix} 0_{9\times l} \\ F^{-1}\left(\mathrm{e}^{FT} - I_l\right)G \end{pmatrix},$$

$$B_d[k] = \begin{pmatrix} B_{d,1}[k] & B_{d,2}[k] \end{pmatrix},$$

$$D_d[k] := \begin{pmatrix} \frac{T^2}{2}\left(g^e(\hat{p}[k]) - 2S(\omega_{ie}^e)v^e[k]\right) \\ T\left(g^e(\hat{p}[k]) - 2S(\omega_{ie}^e)v^e[k]\right) \\ 0_{3\times3} \\ 0_{l\times3} \end{pmatrix}.$$

Then, the state estimate can be recursively propagated by iterating through the time update

$$x^-[k+1] = A_d[k]x^+[k] + B_{d,1}[k]u^*[k] + D_d[k],$$

$$P^-[k+1] = A_d[k]P^+[k]A_d^\mathsf{T}[k] + B_d[k]Q_d[k]B_d^\mathsf{T}[k],$$

many times as necessary. Q_d can be approximated as $Q_d = Q \cdot T$. Alternatively, the term $B_d[k]Q_d[k]B_d^\mathsf{T}[k]$ can be replaced with $\bar{Q}_d$ calculated by using van Loan's method [21, p. 126], from [35].

If all measurements in the vector $y[k]$ were available at time index k, a gain matrix $K_d[k]$ can be calculated in the same way as the discrete-time KF, [3], [5]

$$K_d[k] = P^-[k]C^\mathsf{T}[k]\left(C[k]P^-[k]C^\mathsf{T}[k] + R[k]\right)^{-1},$$

and the updated estimate could be obtained as

$$\hat{x}^+[k] = x^-[k] + K_d[k]\left(y[k] - C[k]x^-[k]\right),$$

$$P^+[k] = (I_{9+l} - K_d[k]C[k])P^-[k].$$

If measurements with indices in the set $\mathcal{I}_k$ are available at time index k, they can be proceed sequentially as follows, [3], [5]. First, use the propagated estimate and covariance,

$$\hat{x}^+[k] \leftarrow x^-[k],$$

$$P^+[k] \leftarrow P^-[k],$$

33

as the starting point for the update loop. Then, for each $i \in \mathcal{I}_k$, where $\mathcal{I}_k$ is set of aiding measurements available at time $t = kT$ in time, loop through the updates

$$K_{d,i}[k] \leftarrow P^+[k]C_i^\mathsf{T}[k]/(C_i[k]P[k]C_i[k]^\mathsf{T} + R_{ii}[k]),$$

$$\hat{x}^+[k] \leftarrow \hat{x}^+[k] + K_{d,i}[k]\left(y_i[k] - C_i[k]\hat{x}^+[k]\right),$$

$$P^+[k] \leftarrow (I_{9+m} - K_{d,i}[k]C_i[k])P^+[k],$$

where C_i is the i-th row of the matrix C, and R_{ii} is the i-th diagonal element of the matrix R. As a result, such implementation yields a corrector-predictor effect where the measurement update is bypassed for all $i \notin \mathcal{I}_k$ corresponding to $K_{d,i}[k] = 0$. A practical consequence is that the elements of the covariance $P[k]$ associated with $i \notin \mathcal{I}_k$, at a given point in time k, increases due to the positive definite process noise covariance matrix $Q_d[k]$ in the time update. Furthermore, for low-frequency measurement updates, the resulting effect is that these are emphasized more at each measurement correction, when available, than high rate measurements. In comparison, the corrector-predictor algorithm of [20, Ch. 11.3.4], for fixed-gain observers, is realized with an explicit time-scale separation where the gain associated with the low-rate measurement i is multiplied with the rate ratio, of the observer relative the aiding sensor, similar to that done in the presentation of the attitude observer discretization. An outline of the implementation of the TMO in direct form, <mark>allowing sequential corrections</mark>, is presented in "Algorithm 2".

Time Delay

If the measurements, typically GNSS and/or magnetometer, [22], used in the NLO experiences a significant time delay, the resetting of the INS state may be a delayed state estimate at the time with index $k - j$ corresponding to the time of validity of the measurement delayed with j samples relative to current time. In this case the INS also contains a "fast-forward" function to rapidly compute the current state estimate based on intermediate IMU measurements. Efficient implementation methods are given in [23], [24] for such problems.

Tightly Coupled Translational Motion Observer

This section introduces the TMO for tightly coupled GNSS/INS integration in detail. The main difference between the loosely and tightly coupled integration is that the aiding sensor information from GNSS changes from the position domain to range domain.

An observer for tightly coupled GNSS/INS integration was presented by [26] where an altered version of the TMO for the loosely coupled observer, (20)–(23), was introduced. In [26], the TMO was integrated with the same attitude observer as presented earlier in this article.

₂₆ Tightly coupled integration utilize the raw GNSS observables, range and range-rate (Doppler) measurements, to alter the TMO injection terms from the position domain to the ₂ range domain. The range measurements y_i can either be pseudoranges, obtained with C/A or other code-phase techniques, or with carrier-phase based ranges, where the subscript i indicate ₄ measurements from the ith satellite. The range-rate measurement is the Doppler frequency ν_i here measured in meters per second.

₆ The range and range-rate measurements are subject to disturbances and errors represented by, for instance, the clock range error β between the atomic satellite clocks and the less accurate ₈ receiver clock. Even a small error in timing can have a large impact as it is multiplied with the speed of light. It is therefore vital that β is estimated in the observer. More on error sources and ₁₀ GNSS/GPS is found in "GNSS – Position Calculation and Error Sources" and "GPS: The First GNSS – Signals and Positioning Services". Other disturbances on the satellite measurements ₁₂ include ionospheric and tropospheric disturbances which delay the signals due to obstructions in the signal path. Such disturbances can be opposed by a dual frequency receiver where a ₁₄ ionospheric-free linear combination of the two frequency measurements (for instance GPS L1 and L2) can be formed. The drawbacks of this approach is the higher cost of receiver and ₁₆ antenna and the increase in noise on the linear combination due to amplification of multipath and receiver noise. Another approach is to utilize a dual receiver configuration where the ₁₈ satellite measurements are differenced with measurements at a known location close by, thereby cancelling the delays. In [36] observers using single- and double-differenced measurements are ₂₀ proposed using an observer structure similar to the one presented here.

Assuming measurements from at least four satellites ($m \geq 4$) are available, the TMO takes

the form of

$$\dot{\hat{p}}^e = \hat{v}^e + \sum_{i=1}^{m} \left(K_i^{pp} e_{y,i} + K_i^{pv} e_{\nu,i} \right), \tag{50}$$

$$\dot{\hat{v}}^e = -2S(\omega_{ie}^e)\hat{v}^e + \hat{f}^e + g^e(\hat{p}^e)$$
$$+ \sum_{i=1}^{m} \left(K_i^{vp} e_{y,i} + K_i^{vv} e_{\nu,i} \right), \tag{51}$$

$$\dot{\xi} = -R(\hat{q}_b^e)S(\hat{\sigma})f_{\text{IMU}}^b$$
$$+ \sum_{i=1}^{m} \left(K_i^{\xi p} e_{y,i} + K_i^{\xi v} e_{\nu,i} \right), \tag{52}$$

$$\hat{f}^e = R(\hat{q}_b^e)f_{\text{IMU}}^b + \xi, \tag{53}$$

$$\dot{\hat{\beta}} = \sum_{i=1}^{m} \left(K_i^{\beta p} e_{y,i} + K_i^{\beta v} e_{\nu,i} \right). \tag{54}$$

The observer structure of (50)–(54) is similar to the loosely coupled equivalent (20)–(23), however it has different injection terms and it includes estimation of the clock error parameter β accounting for synchronization errors between the satellites' and receiver clocks. The clock bias error is the reason why at least four, and not three, satellites are required to calculate the three position coordinates from the pseudoranges. The error is expressed as a time-varying range: $\beta := c\Delta_c$, where c is the speed of light and Δ_c is the clock error. However, due to the injection signals $e_{y,i}$ $e_{\nu,i}$ some colored noise is going to be embedded in β over time. As indicated by (54), β is assumed constant in the deterministic observer design; $\dot{\beta} = 0$. Incorporating this with a minimum variance optimization criterion, similar to (36)–(37), this model might be considered as a Wiener process, $\dot{\beta} = n_c$, in the tuning process, where n_c is considered to be Gaussian white noise with variance σ_c^2 representing the drift rate of the receiver's clock. Hence, the time-varying dynamics of β is captured by the TMO through the injection terms obtained using the raw GNSS observables.

The injection terms of the observer, based on pseudo-range and range-rate measurements, are driven by the errors $e_{y_i} := y_i - \hat{y}_i$ and $e_{\nu,i} := \nu_i - \hat{\nu}_i$, with the estimated measurements

$$\hat{y}_i = \hat{\varrho}_i + \hat{\beta}, \tag{55}$$

$$\hat{\nu}_i = \left(\frac{\hat{p}^e - p_i^e}{\hat{\varrho}_i} \right)^\mathsf{T} (\hat{v}^e - v_i^e), \tag{56}$$

where the position and velocity of the ith satellite are denoted p_i^e and v_i^e. The estimated geometric distance between satellite and receiver is given as $\hat{\varrho}_i = \|\hat{p}^e - p_i^e\|_2$. The estimation errors are defined as $\tilde{p} := p^e - \hat{p}^e$, $\tilde{v} := v^e - \hat{v}^e$, and $\tilde{\beta} := \beta - \hat{\beta}$. When estimating the satellite measurements and geometric distance, the position and velocity of the satellites are assumed known. This

36

assumption is satisfied by using the updated ephemeris data to determine position and velocity of the visible satellite.

Similar to (35) the observer (50)–(54) can be written

$$\dot{\hat{x}} = A\hat{x} + Bu + D(t, \hat{x}) + K(y - h(\hat{x})), \tag{57}$$

however with a nonlinear observation vector $h(\hat{x})$, and the matrices,

$$A = \text{blockdiag}(A^*, 0), \quad B = \begin{pmatrix} B^* \\ 0_{1\times 3} \end{pmatrix},$$

$$D(t, \hat{x}) = \begin{pmatrix} 0_{3\times 1} \\ g^e(\hat{p}^e) - 2(\omega_{ie}^e)\hat{v}^e \\ 0_{3\times 1} \\ 0 \end{pmatrix},$$

where the linearized C matrix,

$$C = \left. \frac{\delta h}{\delta x} \right|_{x=\hat{x}}, \tag{58}$$

takes the form of

$$C = \begin{pmatrix} \frac{(\hat{p}^e - p_1^e)^\intercal}{\hat{\varrho}_1} & 0_{1\times 3} & 0_{1\times 3} & 1 \\ \vdots & \vdots & \vdots & \vdots \\ \frac{(\hat{p}^e - p_m^e)^\intercal}{\hat{\varrho}_m} & 0_{1\times 3} & 0_{1\times 3} & 1 \\ \frac{(\hat{v}^e - v_1^e)^\intercal}{\hat{\varrho}_1} & \frac{(\hat{p}^e - p_1^e)^\intercal}{\hat{\varrho}_1} & 0_{1\times 3} & 0 \\ \vdots & \vdots & \vdots & \vdots \\ \frac{(\hat{v}^e - v_m^e)^\intercal}{\hat{\varrho}_m} & \frac{(\hat{p}^e - p_m^e)^\intercal}{\hat{\varrho}_m} & 0_{1\times 3} & 0 \end{pmatrix}, \tag{59}$$

when using GNSS pseudorange and range-rate measurements. The time-varying C matrix consists of estimated LOS vectors describing the direction from rover to each satellite. As the distance between rover and satellites is large compare to the relative velocity, the LOS vectors are slowly time-varying. As illustrated in Fig. 17 the pseudoranges relate to the position p^e nonlinearly. Hence, the linerization (58) is necessary to obtain C. If the C matrix is applied to the augmented version of (26) with A and B to obtain $P(t)$, the observer gain can be calculated as

$$K = \theta L_\theta^{-1} K^0 E_\theta, \tag{60}$$

with

$$K^0 = PC^\intercal R^{-1}, \tag{61}$$

37

and

$$L_\theta = \text{blockdiag}\left(I_3, \frac{1}{\theta}I_3, \frac{1}{\theta^2}I_3, \frac{1}{\theta^4}\right), \tag{62}$$

$$E_\theta = CL_\theta C^\dagger. \tag{63}$$

The conditions for (50)–(63) are satisfied when four or more pseudoranges are available (except in degenerate configurations), thereby ensuring observability of the system, [26]. In contrast to the loosely coupled GNSS/INS integration, the feedback interconnection of (50)–(54) with the attitude observer, is only locally exponentially stable, with respect to position and velocity initialization errors, since the C matrix is based on linearization of the pseudorange and Doppler measurement equations about the estimated position and velocity. Accurate initialization procedures are easily applied, [26], so this is not a significant problem in practice.

To accommodate colored noise, when applying tightly coupled integration, the R matrix can be increased in an ad hoc manner. An example using such strategy, is designing a tuning rule based on the elevation angle of each satellite in view, [5, Ch. 9.4.2.4]. By doing this, it is possible to weight pseudoranges from low elevation satellites less than measurements from high elevation satellites (with high elevation satellites, the GNSS signal travels through less atmosphere compared to the signals from the low elevation satellites and therefore has less errors).

Augmented TMO for Tightly Coupled Integration Including Clock Error Model

Above, the clock error was modelled in range space as $\beta = c \cdot \Delta_c$ with Δ_c being the clock error. This can be extended further by considering that Δ_c is dependent on the clock frequency error, such that β is no longer considered as a constant, but expressed with a state space model with a constant clock frequency error f_{clock} such that $\ddot{\beta} = 0$, see [3, Ch. 8.4.3.2], [5, Ch 9.4.2.3]:

$$\begin{pmatrix} \dot{\beta} \\ \dot{f}_{\text{clock}} \end{pmatrix} = \begin{pmatrix} 0 & 1 \\ 0 & 0 \end{pmatrix} \begin{pmatrix} \beta \\ f_{\text{clock}} \end{pmatrix} + \begin{bmatrix} 0 \\ n_f \end{bmatrix}, \tag{64}$$

where n_f is the driving process noise assumed to be white. By introducing the additional clock error state, (54) in the TMO is replaced by

$$\dot{\hat{\beta}} = \hat{f}_{\text{clock}} + \sum_{i=1}^{m} \left(K_i^{\beta p} e_{y,i} + K_i^{\beta v} e_{\nu,i} \right), \tag{65}$$

$$\dot{\hat{f}}_{\text{clock}} = \sum_{i=1}^{m} \left(K_i^{fp} e_{y,i} + K_i^{fv} e_{\nu,i} \right). \tag{66}$$

By doing this, (57) is augmented accordingly. With this augmentation, the C-matrix of (59), in (26), is replaced with C_{aug}, given as

$$C_{\mathrm{aug}} = \begin{pmatrix} C & C_{\mathrm{f}} \end{pmatrix},\tag{67}$$

where $C_{\mathrm{f}} = (0_{m\times 1}; 1_{m\times 1})$. The standard deviation of the white noise n_f ought to be chosen small (less than 0.02 m/s as proposed in [3, Ch. 8.4.3.2]). However, by modeling of the clock bias as (64), compared to $\dot{\beta} = 0$ as done in [26], only minor effects (centimeter level) on the estimation of β were observed. Therefore major effects on the position and velocity estimates cannot be expected with this augmentation. Also with this clock error model, it is necessary to take into account that noncompensated common residuals of the time-varying errors due to signal delays, in the ionosphere and troposphere or stemming from multipath, may be embedded in β and f_{clock} since these are the only nuisance parameters related to the GNSS in this TMO.

Indirect Observer Implementation

With the different GNSS/INS integration schemes based on the NLO presented, some further consideration about implementation aspects is discussed in the following section.

INS technology typically utilizes indirect filters, also known as error-state filters, [1], [3], [5]. In such filters/observer implementations, the error between the states of the INS and the corresponding sensor measurements are utilized as states in the error-state filter. Such Kalman filters only run at the frequency of the aiding sensors, hence such filters implementations have lower computational footprint compared to their counterpart, the direct filters. This is due to the covariance equations, with the corresponding matrix operations are propagated at significantly lower rate than the frequency of the INS mechanization. The indirect strategy to solve the GNSS/INS integration problem is also based on complementary filtering, presented earlier in the text.

Indirect Attitude

The attitude in this case is mechanized and provided to the TMO in a dead reckoning fashion at the rate of the IMU as indicated in Fig. 18. The INS mechanization can be made by assuming the angular velocity is constant over the integration interval resulting in

$$\begin{aligned}
R_{b,\mathrm{INS}}^{e}[k] = R_{b,\mathrm{INS}}^{e}[k-1]\Big(& I_3 + TS(\omega_{\mathrm{INS}}^{b}[k]) \\
& - TS(\omega_{ie}^{e})R_{e,\mathrm{INS}}^{b}[k-1]\Big),
\end{aligned}\tag{68}$$

where $\omega_{\mathrm{INS}}^{b}[k] = \omega_{\mathrm{IMU}}^{b}[k] - b_{g,\mathrm{INS}}^{b}[k]$. For this to be an accurate approximation, it is necessary to propagate the attitude at high rates, [37]. This is done to attenuate high-frequency effects

of vibrations and inertial measurements errors, but also to minimize effects from sampling and discretization errors.

The nonlinear attitude observer can be realized in indirect form as shown in Fig. 18. The injection terms are similar to (18)–(19),

$$\hat{\sigma}_1[k] = \frac{\delta t_{\text{acc}}}{T} k_1[k] \, \underline{v_1}^b[k] \times (R_b^e)_{\text{INS}}^{\mathsf{T}}[k] \underline{v_1}^e[k],$$

$$\hat{\sigma}_2[k] = \frac{\delta t_{\text{mag}}}{T} k_2[k] \, \underline{v_2}^b[k] \times (R_b^e)_{\text{INS}}^{\mathsf{T}}[k] \underline{v_2}^e[k],$$

except that the rotation matrix from the INS is applied when calculating $\hat{\sigma}_1[k]$ and $\hat{\sigma}_2[k]$. Moreover, the scaling parameters δt_{acc} and δt_{mag} have the same function as before, however with this realization, the attitude may be propagated with the INS mechanization significantly faster than the estimated attitude is calculated. The attitude estimate may be corrected when a new measurement from the magnetometer or accelerometer is available. Slower frequencies may also be chosen. When a new $\hat{\sigma}[k]$ is calculated, the quaternion $\hat{q}_b^e[k]$ and gyro bias $\hat{b}_g^b[k]$ estimates are calculated using (14) and (16), respectively. Then, the INS's rotation matrix and the gyro bias predictions are reset accordingly,

$$R_{b,\text{INS}}^e[k] \leftarrow R(\hat{q}_b^e[k]),$$

$$b_{g,\text{INS}}^b[k] \leftarrow \hat{b}_g^b[k],$$

as indicated with dashed-doted lines in Fig. 18. If the attitude update is not carried out at every INS sample, $\hat{q}_b^e[k-1]$ has to be calculated from $R_{b,\text{INS}}^e[k-1]$, using for instance Shepperd's algorithm [38], such that

$$\hat{q}_b^e[k-1] \leftarrow R_{b,\text{INS}}^e[k-1],$$

before applying (14), to satisfy the assumption that the angular rates have to be constant between attitude updates.

Indirect TMO

The indirect TMO filter realization is inspired by traditional indirect INS filter mechanizations such as [1] where the structure is similar to Fig. 18. In this case, the state vector of the observer consists of the error between the aiding reference and the INS and colored noise estimate z. First, by defining the INS error vector

$$\delta x^* := \begin{pmatrix} \delta p \\ \delta v \\ \delta \xi \end{pmatrix} = \begin{pmatrix} p^e - p_{\text{INS}}^e \\ v^e - v_{\text{INS}}^e \\ \xi - \xi_{\text{INS}} \end{pmatrix}, \tag{69}$$

40

where INS in subscript indicates the current state of the INS. The indirect filter problem for loosely coupled integration is then implemented using the state vector given as

$$\delta x[k] = \begin{pmatrix} \delta x^*[k] \\ z[k] \end{pmatrix}, \tag{70}$$

including the state augmentation of (35) to take into account that the aiding measurement is subjected to colored noise similar to the *direct* implementation strategy presented earlier. It can be noted that the error state z has no corresponding state in the INS and therefore used directly as a state in the *indirect* implementation. For tightly coupled integration, $z[k]$ represents the chosen state vector of the GNSS clock error model, given as either $z[k] = \beta[k]$ or $z[k] = (\beta[k]\,;\,f_{\text{clock}}[k])$. The corresponding model is then stated as

$$\delta x[k] = A_d[k-1]\delta x[k-1] \\ - B_d[k-1]w[k-1], \tag{71}$$

$$\delta y[k] = C[k]\delta x + \varepsilon_{pv}[k], \tag{72}$$

with $w[k] = \left(\varepsilon_f^b[k],\, S(\hat{\sigma}[k])\varepsilon_f^b[k],\, n[k]\right)^{\mathsf{T}}$. By defining $x_{\text{INS}} := (p_{\text{INS}}^e; v_{\text{INS}}^e; \xi_{\text{INS}})$, the error-state measurement of (72) is obtained for loosely coupled integration as

$$\begin{aligned} \delta y[k] &= y[k] - C^* x_{\text{INS}}[k] + \varepsilon_{pv}[k] \\ &= C^* x[k] + Hz[k] + \varepsilon_{pv}[k] - C^* x_{\text{INS}}[k] \\ &= C[k]\delta x[k] + \varepsilon_{pv}[k], \end{aligned} \tag{73}$$

which is the difference between the aiding sensor and the corresponding INS state. Similar arguments are valid for a tightly coupled integration strategy yielding

$$\begin{aligned} \delta y[k] &= y[k] - h\left(x_{\text{INS}}^*[k]\right) + \varepsilon_{pv}[k] \\ &= h\left(x^*[k]\right) + z[k] + \varepsilon_{pv}[k] - h\left(x_{\text{INS}}^*[k]\right) \\ &= h\left(\delta x[k]\right) + \varepsilon_{pv}[k]. \end{aligned} \tag{74}$$

In contrast to a direct observer structure, the time updates have to be carried out before the measurement update. This is due to the discrete-time model being dependent on the time since the aiding/reference sensor last provided a measurement. This time difference is not necessarily constant from sample to sample.

The indirect TMO time update can be written

$$\delta x^-[k] = A_d[k-1]\delta x^+[k-1], \tag{75}$$

$$P^-[k] = A_d[k-1]P^+[k-1]A_d^{\mathsf{T}}[k-1] \\ + B_d[k-1]Q_d[k-1]B_d^{\mathsf{T}}[k-1], \tag{76}$$

41

with $A_d[k-1] = \mathrm{e}^{A\delta t}$, as presented in (49), where $\delta t = t[k] - t[k-1]$ is the time since the last GNSS measurement was available. Then, with the predictions ahead

$$\delta \hat{x}^+[k] \leftarrow \delta x^-[k], \tag{77}$$

$$P^+[k] \leftarrow P^-[k], \tag{78}$$

the measurement update may be carried out similar to the discrete time realization of the direct TMO filter. After the measurement update, the INS state vector is corrected accordingly,

$$x_{\mathrm{INS}}^+[k] = \begin{pmatrix} p_{\mathrm{INS}}^e[k] + \delta \hat{p}^+[k] \\ v_{\mathrm{INS}}^e[k] + \delta \hat{v}^+[k] \\ \xi_{\mathrm{INS}}[k] + \delta \xi^+[k] \end{pmatrix}, \tag{79}$$

to compensate for the estimation error. After the correction, the error-state estimate vector is reset accordingly,

$$\delta \hat{x}^+[k] = \begin{pmatrix} \delta \hat{p}^+ \\ \delta \hat{v}^+ \\ \delta \xi^+ \\ \hat{z}^+ \end{pmatrix} \leftarrow \begin{pmatrix} 0 \\ 0 \\ 0 \\ \hat{z}^+ \end{pmatrix},$$

since the INS state now accounts for the estimated error. The GNSS error state is not reset to zero since this is an auxiliary state not being part of the INS, as presented in Fig. 18. Therefore, the time update of (75) for position, velocity and the intermediate state ξ, associated with δx^*, is trivial since $\delta(x^*)^+[k-1] \equiv 0$ from time $k-1$ to k due to $\delta(x^*)^-[k] = A_d^* \delta(x^*)^+[k-1] = \delta(x^*)^+[k-1] = 0$ because of the reset, [3, Ch. 4.10 & 5.10.5.3]. Hence, only the time update of the GNSS error is necessary,

$$z^-[k] = A_z[k-1]z^+[k-1], \quad A_z[k-1] = \mathrm{e}^{F\delta t}. \tag{80}$$

The measurement update related to $\delta(\hat{x}^*)^+$ reduces to

$$\delta(\hat{x}^*)^+ = K^*[k]\delta y[k], \tag{81}$$

since $(x^*)^+[k-1] \equiv 0$, while for the error state $z[k]$ the traditional KF measurement update is utilized, taking the form of

$$\delta \hat{z}^+[k] = \delta \hat{z}^-[k] + K_z[k](\delta y[k] - C[k]\delta x^-[k])$$
$$= \delta \hat{z}^-[k] + K_z[k](\delta y[k] - H[k]z^-[k]), \tag{82}$$

for loosely coupled integration and the form of

$$\delta \hat{z}^+[k] = \delta \hat{z}^-[k] + K_z[k]\big(\delta y[k] - h(z^-[k])\big), \tag{83}$$

for tightly coupled integration. Propagation of $P^+[k-1]$ and correction of $P^-[k]$ is independent of resetting and is carried out for all states.

42

The estimation errors in the direct and indirect schemes are defined as, $\tilde{x} := x - \hat{x}$ and $\delta\tilde{x} := \delta x - \delta\hat{x}$, respectively. Both formulations are equivalent as seen by

$$\begin{aligned}
\delta\tilde{x} &= \delta x - \delta\hat{x} \\
&= (x - x_{\text{INS}}) - (\hat{x} - x_{\text{INS}}) \\
&= x - \hat{x} := \tilde{x}.
\end{aligned} \tag{84}$$

Regarding TMOs in PVA estimation, the indirect formulations have some advantages compared to the direct formulation. The indirect scheme is computationally more efficient than the direct counterpart since the time update and the measurement update are performed at the sampling frequency of the aiding sensor. Regarding the time update of the indirect TMO, the term $B_d[k]Q_d[k]B_d^{\mathsf{T}}[k]$ in the covariance update (76) is replaced with $\bar{Q}_d$ when performing the covariance propagation. In [5, Ch. 14.2.6], it is stated that $Q_d \approx Q \cdot T$ if $t[k] - t[k-1] \leq 0.2$ seconds corresponding to a sampling frequency equal or higher than 5 Hz. Since the GNSS measurements are often obtained at a lower frequencies than 5 Hz, it is advised that $\bar{Q}_d$ is utilized and calculated with van Loan's method, as mentioned above. Then, (76) becomes

$$P^-[k] = A_d[k-1]P^-[k-1]A_d^{\mathsf{T}}[k-1] + \bar{Q}_d[k-1], \tag{85}$$

where $A_d[k-1]$ can be time-varying, to account for asynchronous measurement aiding (T is not necessarily constant) since the indirect TMO is only time propagated after a new measurement $y[k]$ is available.

Experimental results

This section presents a comparison of the performance of the discussed observer structures using experimental data collected during a UAV mission.

Experimental verification of the presented observers is carried out using flight data from a UAV test flight, to verify the observers under realistic conditions with fast dynamics. The UAV used is a fixed wing Penguin B UAV configured as listed in Table 1 in the Application Example. The dataset used here has a length of approximately 22 minutes with a flight part consisting of multiple circles and figures-of-eight over an area of one square kilometer.

During the flight, a stationary GNSS receiver of the same type was placed at a known location to serve as base station for a real time kinematic (RTK) positioning solution. The RTK position was computed by the open source software package RTKLIB, [39], where the position is obtained using carrier-phase positioning, with a fixed or float integer ambiguity solution, indicating decimeter accuracy, [5]. The RTK position is used as reference when comparing the

performance of the loosely and the tightly coupled observer structures. The base station also logged the transmitted satellite ephemeris data, used to calculate the satellites' positions and velocities. RTK is a type of differential GNSS. For details on differential GNSS, see "GPS: The First GNSS – Signals and Positioning Services".

The loosely and tightly coupled observers are compared. To guarantee a fair comparison, the standalone GNSS position solution used in the loosely coupled integration is based on the tightly coupled observer using solely the pseudoranges as observables. Hence, no IMU is used to generate this aiding position solution.

The tuning parameters for the observers are gathered in the Q and R matrices for gain selection. For the loose integration, the matrices are: $Q_l = \mathrm{blockdiag}(0_{3\times3}, 10^{-10} \cdot I_3, 2.5 \cdot 10^{-3})$, $R_l = \mathrm{blockdiag}(2.5 \cdot I_3)$. For the tightly coupled integration, the tuning matrices are: $Q_t = \mathrm{blockdiag}(Q_l, 1)$, $R_t = \mathrm{blockdiag}(1 \cdot I_m)$. The observers use the same constant attitude estimator gains: $k_I = 0.004$, $k_1 = 0.25$, and $k_2 = 0.75$.

The comparison of the observers are seen in Fig. 19, depicting the position estimation error. Fig. 20 shows the estimated attitude, while Fig. 21 displays the estimated gyro bias. The position estimation is evaluated in terms of root-mean-square error (RMSE) and standard deviation (STD) relative to the RTK solution and summarized in Table 2.

As presented above, tuning of the Q matrix associated with the velocity state is based on statistics describing the accelerometer's noise characteristics. These can either be based on the data collected or from a data sheet. For a standalone GNSS solution (IMU not used), tuning of the Q matrix reduces to an ad hoc procedure based on the assumed host-vehicle dynamics. [5, Ch. 9.4] recommends $1^2 \, \mathrm{m/s^2}$, $10^2 \, \mathrm{m/s^2}$ and $100^2 \, \mathrm{m/s^2}$ for pedestrian, automotive and military aircraft, respectively associated with the velocity state.

TABLE 2: Navigation performance comparison

	RMSE (x,y,z) [m]			STD (x,y,z) [m]		
Tightly coupled	3.412	3.341	1.106	1.067	0.561	1.005
No IMU	4.541	3.732	2.184	2.951	1.756	2.065
Loosely coupled	4.442	3.818	2.264	2.836	1.868	2.177

As seen in Fig 19, the tightly coupled GNSS/INS integration strategy provides the position estimates with smallest variation and also the smallest deviation from the RTK positioning

solution. This statement is backed up by Table 2. The difference between a standalone GNSS solution and loosely coupled integration seems less evident form Fig. 19 and Table 2. This is however expected, taking into account the simulation results related to the loosely coupled GNSS/INS integration and the estimation of colored GNSS noise presented earlier. The benefit of loosely coupled integration, relative not using an IMU at all, is however evident in Fig. 22. The loosely coupled solution provides a smoother estimate than the standalone GNSS solution and is hence more suitable to be used in an autopilot that operate at high sampling rate. The INS also provides fault tolerance when GNSS fails or is degraded. Moreover, one large benefit of loosely coupled GNSS/INS, relative to a standalone GNSS solution, is that the attitude estimates also are obtained with high accuracy.

As mentioned, the most accurate and precise position estimates relative to the RTK solution are obtained with the tightly coupled integration strategy. Since the pseudoranges are directly fused with the inertial measurements, instead of calculating the GNSS position before using this as aid in loosely coupled integration, more of the colored noise, embedded in the GNSS pseudoranges, is captured by the receiver's clock bias estimate. This is possible since the acceleration measurements are available between GNSS samples. Hence, every new position and clock error calculation, made by the observer, is based on the current predicted position between GNSS samples using inertial data rather than using a 0.2 to 1 second old estimate obtained at the previous GNSS update. This point however, is mainly relevant for low-cost GNSS receivers, as higher grade receivers can output raw data at frequencies of 20 Hz or more. A contributing factor to the performance differences of the two integration schemes may also be due to the 5 Hz GNSS update. By sampling the GNSS that fast, more of the pseudorange measurements can become correlated in time compared to using 1 Hz position calculation. If differential GNSS is utilized, more accurate position estimates can be obtained for both integration schemes. For details related to differential GNSS, see "GPS: The First GNSS – Signals and Positioning Services".

The attitude estimates obtained with both loosely and tightly coupled integration are mostly similar except from a few significant differences. These differences are most likely due to the attitude estimate $\hat{q}_b^e$ has two components, the unit quaternion from BODY to NED q_b^n and the unit quaternion from NED to ECEF q_n^e and how the GNSS information enters the TMOs. The latter quaternion q_n^e is in principle a horizontal position estimate containing information of the craft's latitude and longitude. Therefore, the attitude estimates from the two integration strategies may differ as a result of the difference in how the position information enters the TMO due to the feedback interconnection with the attitude observer and the TMO through the auxiliary state ξ. This again will also affect the gyro bias estimation, seen in Fig. 21, and therefore explaining that the estimates obtain using tightly coupled GNSS/INS integration resulted in more steady

estimates compared to applying loosely coupled integration.

Conclusions

Accurate and precise position, velocity and attitude estimates are needed in numerous areas such as the automotive, robotics, marine and aircraft applications. The need for computationally efficient and robust algorithms achieving this is growing due to a wide-spread interest in unmanned platforms, such as unmanned aerial vehicles, with potential limited computational power available. This need can be met by applying nonlinear feedback-interconnected observers for integrated GNSS/INS navigation with known stability properties.

The experimentally verified simulation results, using data collected during a unmanned aerial vehicle flight, show that the estimation of translational motion (position and velocity) benefits from a minimum-variance-like implementation applying the Riccati equation. Using such an implementation strategy, compared to a fixed-gain strategy, accelerates the observers convergence. This is also reflected in the attitude estimates due to the feedback-interconnection relating the two observers. Furthermore, by using an indirect filter implementation, the computational burden of estimating position and velocity is reduced. This is due to the fact that the Riccati equation is updated at the speed of the aiding measurements, in contrast to a direct filter, where the time update of the Riccati equation is implemented at the rate of the inertial measurements.

The attitude estimates are obtained with an exponentially stable and computationally efficient observer based on complementary filtering and vector measurements. In contrast to the Kalman filter, this is not a stochastic method, but based on the desired observer bandwidth and nonlinear stability theory. An indirect observer implementation for the attitude estimation is also proposed. This structure enables the possibility to not necessarily calculate the attitude correction at every measurement sample from the inertial measurement unit, while still maintaining the INS's structure.

The results presented here indicate that tightly coupled GNSS/INS integration outperforms loosely coupled integration when considering position accuracy. By fusing the pseudorange measurements directly with the inertial data, more of the colored noise embedded in the pseudoranges is captured by the receiver's clock error estimate, compared to that achieved with the augmented loosely coupled integration scheme posed.

The attitude estimates obtained with both loosely and tightly coupled integration are mostly similar. Differences are possibly due to the different amount of colored noise being fed from

the respective translational motion observer to the attitude observer.

Accuracy of the loosely and tightly coupled integration schemes can be increased by applying pseudorange corrections using differential GNSS, carrier-phase smoothed pseudoranges or dual-frequency solutions canceling the ionospheric delay at the expense of increased noise.

Acknowledgments

References

[1] P. S. Maybeck, *Stochastic Models, Estimation and Control.* NY: Academic Press, New York 1979.

[2] R. Titterton and J. L. Weston, *Strapdown inertial navigation technology*, 2nd ed. London: Institution of Engineering and Technology, 2004.

[3] J. A. Farrell, *Aided Navigation. GPS with high rate sensors.* McGraw-Hill, 2008.

[4] M. Grewal, L. R. Weill, and A. P. Andrews, *Global positioning systems, inertial navigation and integration*, 3rd ed. Hoboken, New Jersey: John Wiley & Sons Inc, 2013.

[5] P. D. Groves, *Principles of GNSS, Inertial, and Multisensor Integrated Navigation Systems*, 2nd ed. Artech House, 2013.

[6] F. Markley, "Attitude error representation for kalman filtering," *J. Guidance, Control and Dynamics*, vol. 26, pp. 311–317, 2003.

[7] S. J. Julier and J. K. Uhlmann, "Unscented filtering and nonlinear estimation," *Proceedings of the IEEE*, vol. 92, no. 3, pp. 401–422, Mar 2004.

[8] P. M. Djuric, J. H. Kotecha, J. Zhang, Y. Huang, T. Ghirmai, M. F. Bugallo, and J. Miguez, "Particle filtering," *IEEE Signal Processing Magazine*, vol. 20, no. 5, pp. 19–38, Sept 2003.

[9] S. Salcuedan, "A globally convergent angular velocity observer for rigid body motions," *IEEE Trans. Automatic Control*, vol. 36, no. 12, pp. 493–1497, 1991.

47

[10] B. Vik and T. I. Fossen, "A nonlinear observer for GPS and INS integration," in *Proc. IEEE Conf. Decision and Control*, Orlando, FL, 2001, pp. 2956–2961.

[11] R. Mahony, T. Hamel, and J.-M. Pflimlin, "Nonlinear complementary filters on the special orthogonal group," *IEEE Trans. Automatic Control*, vol. 53, pp. 1203–1218, 2008.

[12] M.-D. Hua, "Attitude estimation for accelerated vehicles using GPS/INS measurements," *Control Engineering Practice*, vol. 18, pp. 723–732, 2010.

[13] P. Batista, C. Silvestre, and O. J. Oliveira, "GES attitude observers - Part I: Multiple general vector observations," in *Proc. IFAC World Congress*, Milan, 2011, pp. 2985–2990.

[14] P. Batista, C. Silvestre, and P. Oliveira, "Sensor-based globally asymptotically stable filters for attitude estimation: Analysis, design, and performance evaluation," *IEEE Transactions on Automatic Control*, vol. 57, no. 8, pp. 2095–2100, Aug 2012.

[15] H. F. Grip, T. I. Fossen, T. A. Johansen, and A. Saberi, "Attitude estimation using biased gyro and vector measurements with time-varying reference vectors," *IEEE Trans. Automatic Control*, vol. 57, pp. 1332–1338, 2012.

[16] ——, "Nonlinear observer for GNSS-aided inertial navigation with quaternion-based attitude estimation," in *Proc. American Control Conference*, Washington DC, 2013, pp. 272–279.

[17] ——, "Globally exponentially stable attitude and gyro bias estimation with application to GNSS/INS integration," *Automatica*, vol. 51, pp. 158–166, 2015.

[18] M. Zamani, J. Trumpf, and R. Mahony, "Minimum-energy filtering for attitude estimation," *IEEE Transactions on Automatic Control*, vol. 58, pp. 2917–2921, 2013.

[19] M.-D. Hua, G. Ducard, T. Hamel, R. Mahony, and K. Rudin, "Implementation of a nonlinear attitude estimator for aerial robotic vehicles," *IEEE Transactions on Control Systems Technology*, vol. 22, pp. 201–213, 2014.

[20] T. I. Fossen, *Handbook of Marine Craft Hydrodynamics and Motion Control*, 1st ed. John Wiley & Sons Ltd, 2011.

[21] R. G. Brown and P. Y. C. Hwang, *Introduction to Random Signals and Applied Kalman Filtering: with Matlab Exercises*, 4th ed. Hoboken, New Jersey: John Wiley & Sons Inc, 2012.

[22] J. M. Hansen, T. I. Fossen, and T. A. Johansen, "Nonlinear observer for INS aided by time-delayed GNSS measuements: Implementation and UAV experiments," in *Proc. International Conference Unmanned Aircraft Systems (ICUAS)*, Denver, Colorado, June 9–12 2015, pp. 157–166.

[23] A. Khosravian, J. Trumpf, R. Mahony, and T. Hamel, "Velocity aided attitude estimation on SO(3) with sensor delay," in *Proc. IEEE Conf. Decision and Control*, Los Angeles, CA, Dec. 15–17 2014, pp. 114–120.

[24] ——, "Recursive attitude estimation in the presence of multi-rate and multi-delay vector

measurements," in *Proc. American Control Conference*, Chicago, IL, July 1–3 2015, pp. 3199–3205.

[25] R. H. Rogne, T. H. Bryne, T. A. Johansen, and T. I. Fossen, "Fault detection in lever-arm-compensated position reference systems based on nonlinear attitude observers and inertial measurements in dynamic positioning," in *Proc. of the American Contr. Conf.*, Boston, Ma, 2016.

[26] T. A. Johansen and T. I. Fossen, "Nonlinear observer for inertial navigation aided by pseudo-range and range-rate measurements," in *Proc. European Control Conference*, Linz, Austria, July 15–17 2015, pp. 1673–1680.

[27] H. F. Grip, A. Saberi, and T. A. Johansen, "Observers for interconnected nonlinear and linear systems," *Automatica*, vol. 48, pp. 1339–1346, 2012.

[28] K. R. Britting, *Inertial Navigation Systems Analysis*. John Wiley & Sons Ltd, 1971.

[29] H. D. Black, "A passive system for determining the attitude of a satellite," *AIAA Journal*, vol. 2, no. 7, pp. 1350–1351, 1964.

[30] R. E. Kalman and R. S. Bucy, "New results in linear filtering and prediction theory," *Trans. ASME, Ser. D, J. Basic Eng*, pp. 95–109, March 1961.

[31] H. Vermeille, "Computing geodetic coordinates from geocentric coordinates," *Journal of Geodesy*, vol. 78, pp. 94—95, 2004.

[32] J. Rankin, "GPS and differential GPS: An error model for sensor simulation," in *IEEE Position Location and Navigation Symposium*, Las Vegas, NV, 11–15. Apr 1994, pp. 260–266.

[33] S. C. Mohleji and G. Wang, "Modeling ADS-B position and velocity errors for airborne merging and spacing in interval management application," Available online at http://www.mitre.org/publications/technical-papers/, The MITRE Corporation, 7515 Colshire Drive, McLean VA 22102, September 2010 (last accessed Des, 2015).

[34] R. W. Beard and T. W. McLain, *Small Unmanned Aircraft: Theory and Practice*. Princeton University Press, 2012.

[35] C. F. van Loan, "Computing integrals involving the matrix exponential," *IEEE Trans. Automatic Control*, vol. AC–23, no. 3, 1978.

[36] J. M. Hansen, T. A. Johansen, and T. I. Fossen, "Tightly coupled integrated inertial and real-time-kinematic positioning approach using nonlinear observer," in *Proc. of the American Contr. Conf.*, Boston, Ma, 2016.

[37] A. D. King, "Inertial navigation – forty years of evolution," *GEC*, vol. 13, no. 3, 1998.

[38] S. W. Shepperd, "Quaternion from rotation matrix," *Journal of Guidance and Control*, vol. 1, no. 3, pp. 223–224, 1978.

[39] "RTKLIB, version 2.4.2," Available online at http://www.rtklib.com, Last updated: 29.04.2013.
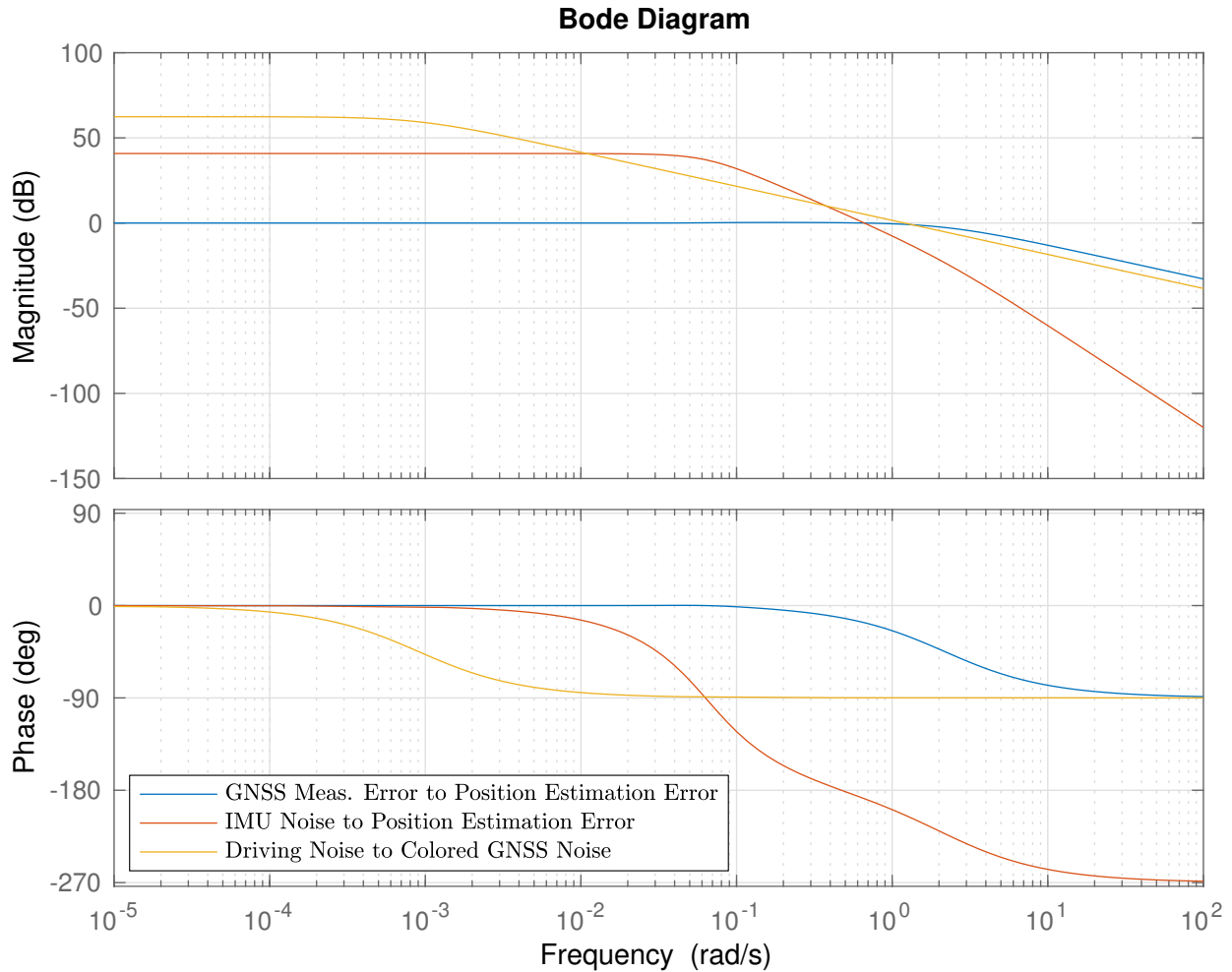
Figure 16: Bode plot. Three bode plots are shown; the transfer function from the GNSS measurements error to the position measurement error is shown in blue, the transfer function from the IMU noise to the position estimation error is shown in red and the transfer function from the driving noise of the global navigation satellite system (GNSS) error model to the colored GNSS position noise model output is shown in yellow. From the three frequency responses, the conclusion is that the bandwidth of the navigation system is higher than the slowly-varying colored noise component embedded in the GNSS position measurements. Due to this, the observer struggles to estimate the GNSS's colored noise correctly.
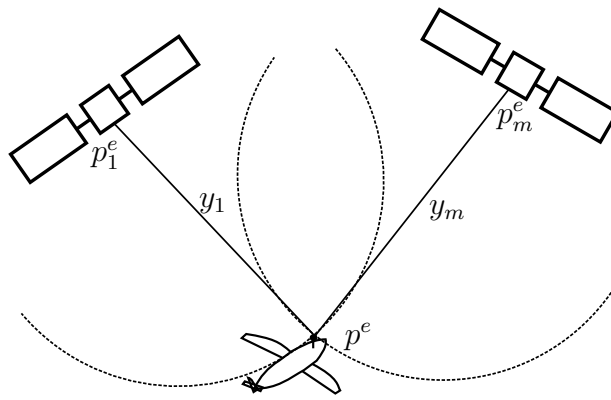
Figure 17: Concept illustration of the ranging done in global navigation satellite systems (GNSS). The receiver position is denoted p^e, while the satellite positions are denoted p^e_i, where $i \in [1, \ldots, m]$. The position of the GNSS receiver may be located anywhere along the circles with radius y_i and origin p^e_i. Because of this, the (pseudo)ranges y_i relate to position of the receiver p^e nonlinearly. The figure is a simplification. With pseudoranges $y_i = \varrho_i + \beta$, where $\varrho_i = \|p^e - p^e_i\|_2$ are the geometric distances between the receiver and the satellites and β being the receiver's clock error multiplied with the speed of light, the nonlinearities become hyperbolic for $\beta > 0$, not circular as indicated.
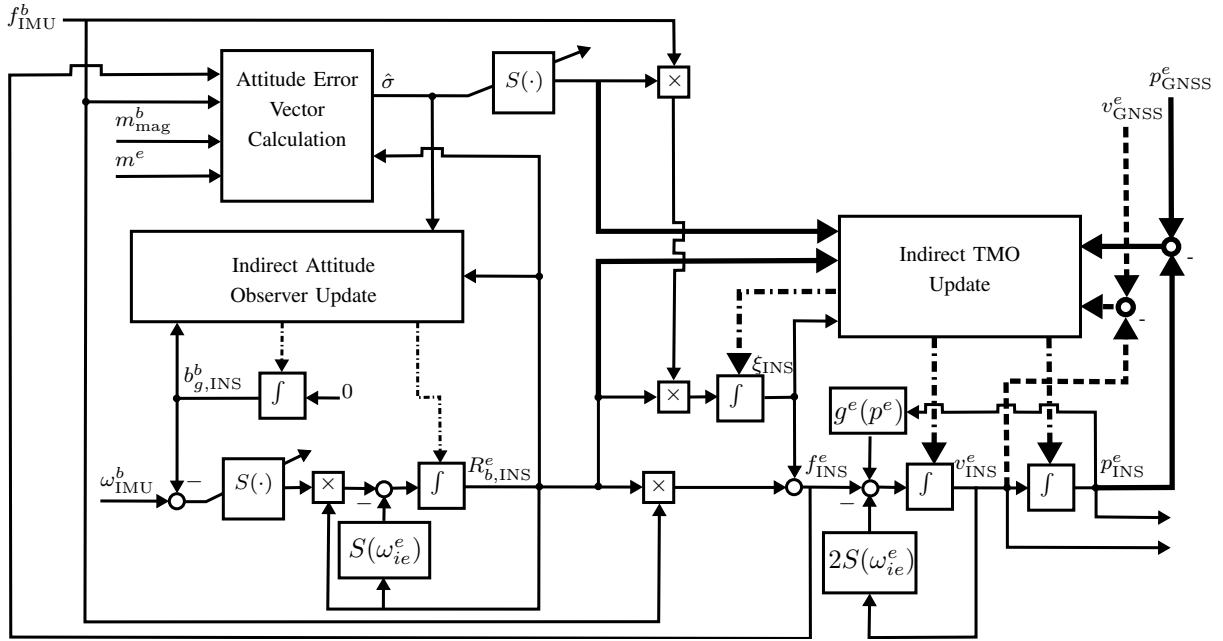
Figure 18: Indirect observer structure. The block diagram illustrates the indirect information flow in a discrete-time implementation of the inertial navigation system (INS) related to both the nonlinear attitude observer and the translational motion observer (TMO). Loosely coupled integration is depicted. The thin lines represent the fastest sampling rate, that of the inertial measurement unit (IMU), the thick lines represent the slowest sampling rate of the global navigation satellite system (GNSS). The estimator state resetting is represented by dash-dot lines. The discrete integration/time update is denoted with the integration symbol $\int$ and is conducted at the fastest sampling rate. The dashed lines related to the GNSS velocity measurements represent optional aiding.
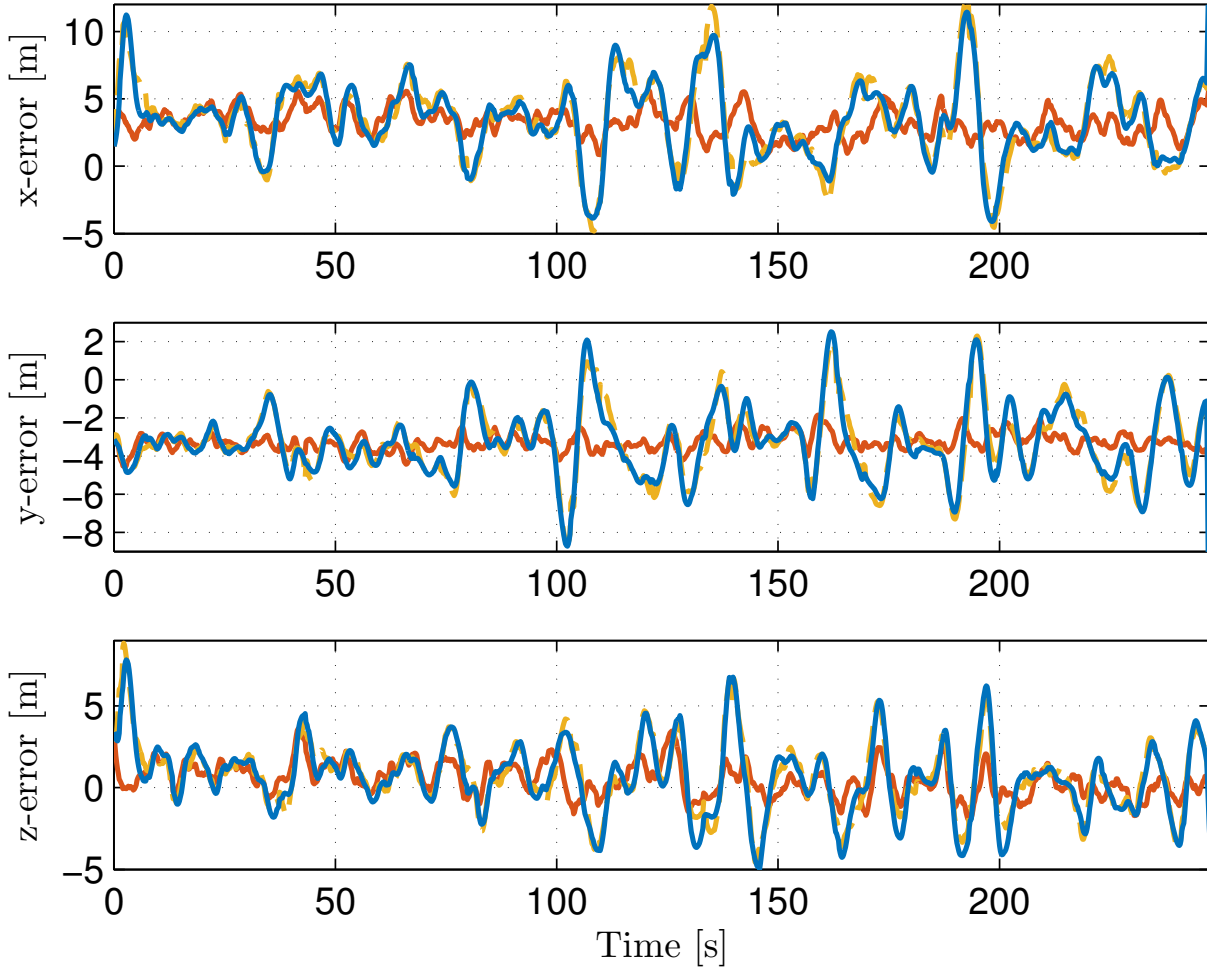
Figure 19: Position estimation error. The results are presented in the Earth-Centered-Earth-Fixed (ECEF) frame relative the real time kinematic (RTK) global navigation satellite System (GNSS) positioning solution. The result obtained using loosely coupled integration is shown in blue, the result obtained using tightly coupled integration is shown in red, while the standalone GNSS solution is presented in yellow. These results indicate that tightly coupled integration of inertial and GNSS measurements yield more accurate position estimation compared to loosely coupled integration and standalone GNSS when applying satellite-based navigation based on the standard GNSS positioning service.
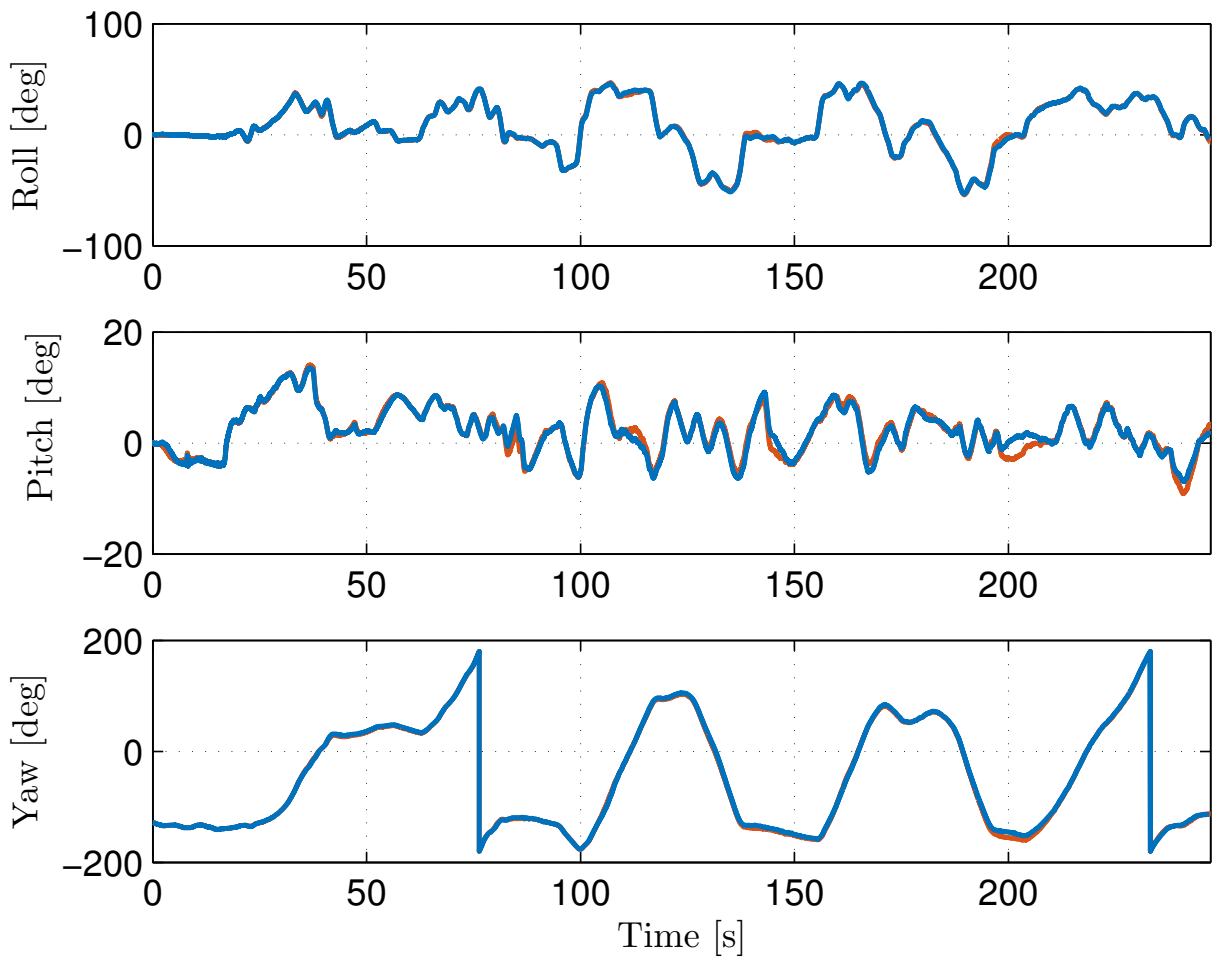
Figure 20: Attitude estimation. The results are presented using Euler angles as attitude representation. The estimate obtained using loosely coupled integration is shown in blue, while the estimate obtained using tightly coupled integration is shown in red. The standalone GNSS navigation solution did not provide attitude estimates.
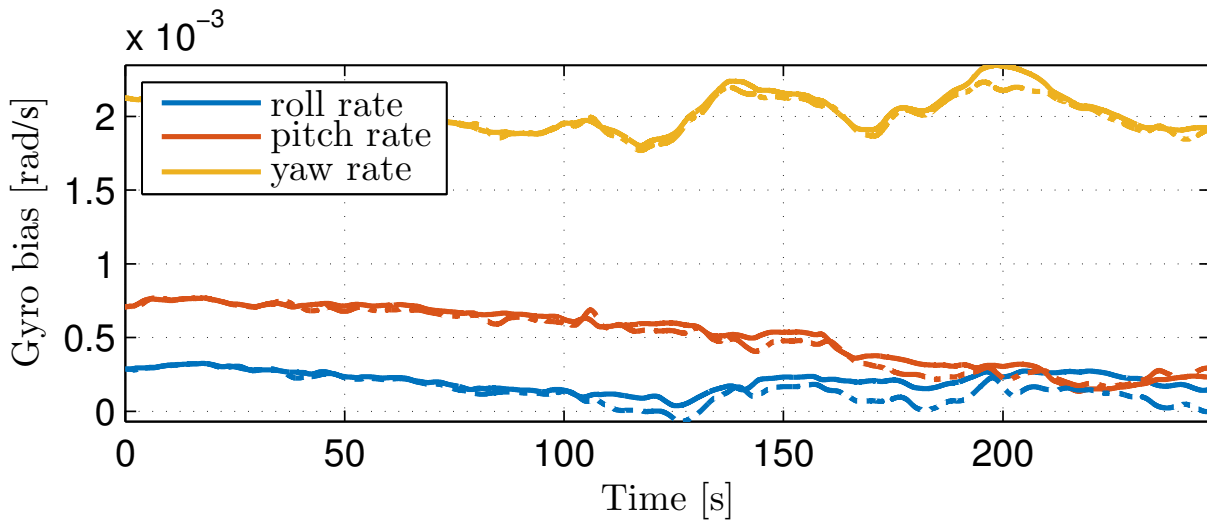
Figure 21: Gyro bias estimation. The result obtained using loosely coupled integration is shown with dotted lines, while the result obtained using tightly coupled integration is shown with solid lines.
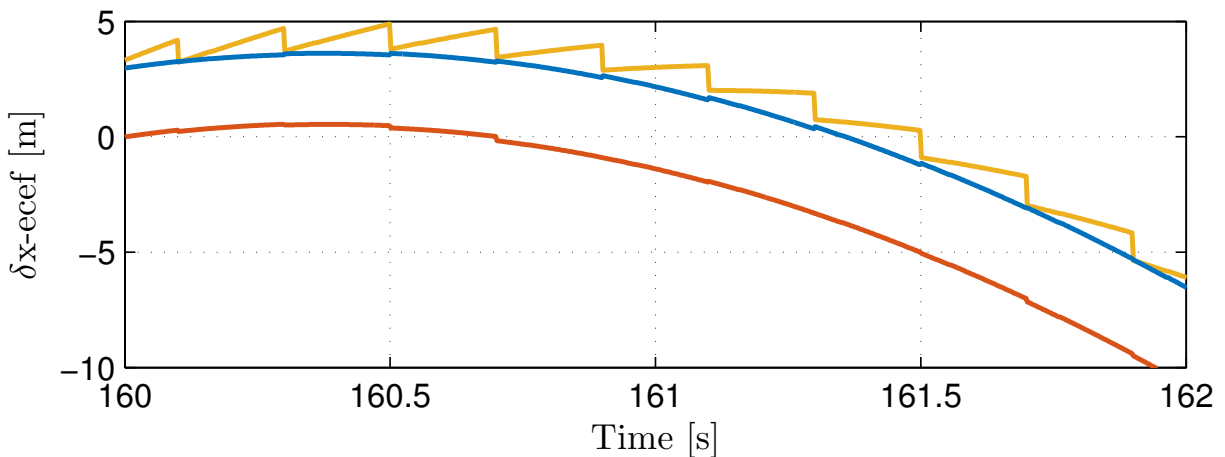

Figure 22: Normalized position error. The results are related to the real time kinematic (RTK) global navigation satellite system (GNSS) positioning solution between 160 and 162 seconds of flight. The error relative the RTK solution applying the loosely coupled integration is shown in blue and the error relative the RTK solution applying the tightly coupled integration is shown in red, while the error relative RTK using pure GNSS positioning is shown in yellow. The error relative RTK is smallest applying tightly coupled integration. The error using loosely coupled integration and pure GNSS is of similar magnitude, however, the integrated solution is smoother than pure GNSS since inertial data is available between GNSS samples.

Sidebar 1: Complementary Filtering

The basic concept of complementary filtering is that a set of measurements are low-pass filtered, while the remaining measurements are high-pass filtered. Because of this, complementary filtering is particularly useful for fusing measurements (or information) with complementary spectral noise characteristics. Inertial sensors and aiding sensors, such as GNSS, have these complementary properties. GNSS is then used to capture the low frequency vehicle motion, while the inertial sensors are used to capture any high frequency vehicle dynamics. For both attitude and heading reference systems (AHRS) and complete INS, complementary filtering is commonly utilized [3, Ch. 4.10], [11], [17]. The general structure of complementary filtering for INS is illustrated in Fig. S1, while the simplified structure for attitude estimation, also known as filtering on $SO(3)$, is presented in Fig. S2.
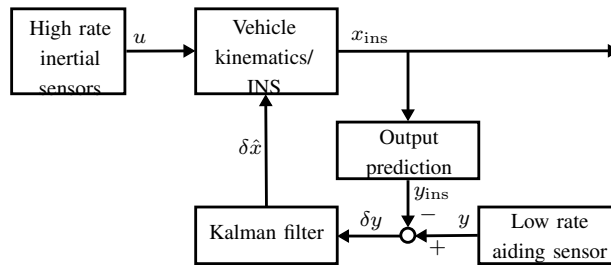

Figure S1: Traditional complementary filtering using the Kalman filter. The structure is also known as error-state or indirect Kalman filtering. The Kalman filter estimates the error between the inertial navigation system (INS) and low rate aiding sensor. For low frequencies, the aiding sensor is the dominating information sensor for the INS output. For high frequencies the high-frequency input from the inertial sensor is the dominating information source in producing the INS output.
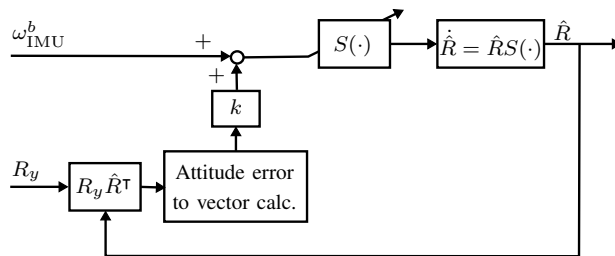
Figure S2: Simplified concept of complementary filtering on $SO(3)$. Some reconstructed attitude measurement $R_y \approx R$ is valid for low frequencies. For frequencies lower than the cut-off frequency k, R_y is the dominating information used to calculate $\hat{R}$. For high-frequencies ω_{IMU}^b is the dominating factor. By using complementary filtering on $SO(3)$, the effect of the low-frequency gyro bias on the attitude estimate is attenuated.

Sidebar 2: History of Global Navigation Satellite Systems

The first GNSS service, the Global Positioning System (GPS) was commenced in 1978 with the first prototype satellites and was initially designated to provide the United States' armed forces with a global positioning system. After the Korean Air Lines Flight 007 accident west of Sakhalin Island in 1983, GPS was authorized for civilian use as well. In 1994 the GPS system was fully operational with 24 satellites in orbit guaranteeing a world-wide coverage. One year later the Russian GLONASS system was fully operational. From 1994 to 2000, the precision obtained from civilian GPS was in the region of 50 meter accuracy horizontally and 100 meters vertically. This artificial degradation of the position precision is known as *selective availability* (SA). In 2007 it was announced that the future GPS Block III satellites will be incompatible with SA, hence making the termination of SA permanent.

Currently two other global satellite navigation systems are under development. These are the Chinese BeiDou Navigation Satellite System and the European Galileo system. For details on GNSS and radiopositioing in general, see [5, Ch. 8].

Sidebar 3: GNSS – Position Calculation and Error Sources

GNSS are ranging systems. The user position is obtained based on multilateration using calculated ranges from the satellites in view. The range calculation is done by obtaining the traveling time of the signal from the satellite to the receiver and multiplying this time with the speed of light. Since the range calculation is corrupted by different errors sources, these ranges are often referred to as *pseudoranges*. The error sources affecting the position calculation can be divided into three main sources;

- satellite errors,
- signal propagation errors and
- receiver errors.

The satellite errors can be divided into satellite clock errors and ephemeris data errors. Propagation errors are due to signal delay in the atmosphere (ionosphere and troposphere). Receiver errors mainly consist of noise as a result of thermal noise, signal processing, clock error and multipath error. Multipath errors are due to GNSS signals reflecting off nearby surfaces before arriving at the receiver. In particular multipath and the ionospheric delays contribute to colored noise being embedded in the receiver's position calculation. The ephemeris data is needed to calculate the user's position (based on the pseudoranges) since the model is based on the knowledge of the respective satellites' positions. Since the clock in GNSS user equipment is of low cost, the receiver's clock error is also estimated. Therefore four or more satellites in view are required to estimate the position on the Earth in ECEF coordinates (together with the receiver's clock error). The solution is based on linearizing the obtained pseudoranges with respect to the user's presumed current position. Usually the position solution is obtained using a Least Squares approach or an extended Kalman filter. For more information on GNSS errors and calculation of position, see [5, Ch. 9], [4, Ch. 6].

Sidebar 4: GPS: The First GNSS – Signals and Positioning Services

Currently the civilian GPS system broadcasts on three frequencies 1575.42 MHz, 1227.60 MHz and 1176.45 MHz. The two former is known as the L1 and L2 frequencies, respectively. The latter is called the L5 frequency. The position measurements is primarily obtained by tracking the code(s) of the GPS system modulated on top of carrier wave generated by at each satellite.

The legacy GPS used two codes, namely the; *Coarse/acquisition* (C/A) and the *precise* code P. The C/A code is modulated on the L1 carrier, while the P code is modulated on both the L1 and L2 carrier. In 2014, the US Air Force began to broadcast the new civilian $L2C$ and $L5$ signals in test mode from block IIF satellites. The $L2C$ and $L5$ codes are attended for the next generation GPS satellites, known as block III. For details related to the GPS signals and codes, see [4, Ch. 4.1.]

On average, depending on atmospheric effects, satellite and multipath errors, a ranging error of 8-11 meters is obtained using the L1 C/A code to calculate the pseudoranges. A horizontal position with RMS precision of 3-5 meters can be expected in such cases, depending on receiver type. Vertically this can be more than twice that due to the satellite geometry being worse vertically than horizontally since the Earth blocks the signals that could increase the vertical position accuracy. Using the C/A code for positioning is referred to as the *standard positioning service* (SPS). With SPS, especially with receiver sampling frequencies faster than $2\,\text{Hz}$, the position error is going to be time-correlated. More information on GNSS, and in particular GPS, can be found in [3, Ch. 8], [4, Ch 1–2], and [5, Ch. 8].

Atmospheric errors, satellite orbit error or satellite clock offset error are spatially and temporally correlated. The differential GNSS (DGNSS) approach is based on the assumption that two closely spaced receivers tracking the same signals at the same time undergo approximately the same error. Thus by differencing measurements from two close and synchronized receivers, spatially correlated errors can be minimized. In DGNSS, the base station calculates pseudorange and range rate corrections for each satellite in view that are broadcasted to the user receiver. With DGNSS (or DGPS), the 3-5 meters RMS error can be reduced to 1-2 meters by applying pseudorange and range-rate corrections from the base station before calculating the user's position. Additionally, there exist several satellite-based augmentation systems (SBAS), such as the US Wide Area Augmentation System (WAAS), European Geostationary Navigation Overlay Service (EGNOS) and others, that can also improve GNSS positioning accuracy. If DGNSS is not sufficient, real time kinematic (RTK) positioning can be applied. RTK approach is based on the same principle as DGNSS. The major difference is that this technique also uses carrier-based ranges for position estimation that provide much higher accuracy than code-based positioning

and that the receiver and base station is time synchronized. To take advantage of the precision of carrier-based measurements, RTK requires raw GNSS measurements to be transmitted from the base station to the user. Additionally, a process called ambiguity resolution is required to determine the initial integer number of whole cycles. The RTK approach is capable of providing positioning accuracy on a centimeter level if the integer ambiguities are successfully resolved. For more information on DGNSS and RTK, [3, Ch. 8.8], [4, Ch. 8], and [5, Ch. 10], can be advised.

GNSS velocity measurements may be obtained based on differences of the position solution. This however has become a dated technique for determining the velocity of a craft exposed to medium and high dynamics. The user's velocity can be obtained from the receiver's internal EKF. Using Doppler observables, in addition to the pseudoranges, further improves the velocity precision and accuracy. Doppler-based velocity determination is inherently more accurate and yields a much faster response to user dynamics than position differences, [4, Ch. 6.4.5]. When using Doppler measurements, a velocity RMS error of 0.1-1 m/s can be expected depending on conditions (obstructions, satellite geometry, etc.). Although the Doppler-based velocity solution is accurate, it is not without some dynamics since the measured Doppler shift is not a raw measurement, but derived as the deviation from the nominal carrier frequency. Therefore, the Doppler shift is a function of the user's velocity, the satellite velocity, the line-of-sight (LOS) vector to the satellite (derived using the pseudorange measurements and the satellites' positions), the carrier wave length and the receiver's clock frequency, [4, Ch. 6.3.3 & Ch. 6.4.5]. Due to the low-cost clocks in GNSS user equipment, the clock error (β is this article) is not constant since the clock's oscillator frequency is not constant. The LOS vector from satellite to receiver also is affected by time-correlated pseudorange noise. An alternative way to measure the Doppler shift is to count the cycles of the carrier in the receiver over a shorter time window (1s or less is common). In either case, the Doppler shift is obtained based on the assumption that the receiver's clock frequency has no error. Hence, the velocity error is going to contain colored noise components. For more information on the Doppler range-rate measurement, [4, Ch. 6.4.5] and [5, Ch 9.2.7], can be advised.

Sidebar 5: Inertial Measurement Units

An inertial measurement unit (IMU) is a sensor providing measurements of angular rate and specific force in three axes. The angular rates, measured in the BODY frame, are relative the inertial frame,

$$\omega_{\text{IMU}}^b = \omega_{ib}^b + b_g^b + \varepsilon_g, \tag{S1}$$

whilst the specific force is measured as the sensor's acceleration minus the gravity,

$$f_{\text{IMU}}^b = a_{ib}^b - (R_b^e)^\intercal g^e(p^e) + b_f^b + \varepsilon_f, \tag{S2}$$

where R_e^b is the rotation matrix from BODY to the ECEF frame. The b_*^b and ε_* terms in (S1)–(S2) represents sensor biases and sensor noise. The magnitude of these error sources are affected by the underlying sensor technology. The main IMU technologies are summarized in Table S1. For further details on IMUs and inertial sensor technology, see [2] and [4].

TABLE S1: IMU and Inertial Sensor Technology

Angular rate/Gyro	Accelerometer
Momentum wheel (used for instance in gyrocompassing)	Gyroscopic (mass displacement detection)
Optical (based on laser or fiber optic technology)	Pendulous (mechanical)
Coriolis/vibratory gyros (MEMS)	Vibratory accelerometers (MEMS)

An increasingly popular type of IMUs are units based on micro-electro-mechanical-systems (MEMS) technology. These are small and lightweight, with a reasonable measurement quality, providing the user with a cost-effective solution.

Some IMUs have embedded magnetometers and a barometer, enabling the user to obtain additional information related to the vehicle's heading and altitude, in a single unit. An alternative source of heading determination is based on mechanical gyroscopic technology, known as a mechanical gyrocompass. This is a mechanical unit which orientation is fixed in space such that the vehicle's attitude is obtained by reading the unit's angles relative its mounting frame.

Sidebar 6: Algorithm 1

Algorithm 1 Discrete-time attitude observer in direct form.

Require: Initializing the observer,

1: $\hat{q}_b^e[0] = q_0(\phi[0], \theta[0], \psi[0])$, $\hat{b}_g^b = 0_{3\times1}$, where q_0 is the mapping from the initial Euler angles $\phi[0], \theta[0], \psi[0]$.

2: Enforcing $\|\hat{q}_b^e[0]\| = 1$, using $\hat{q}_b^e[0] = \hat{q}_b^e[0]/\|\hat{q}_b^e[0]\|$.

3: Extracting $s_q[0]$ and $r_q[0]$ from $\hat{q}_b^e[0]$ and calculating the initial rotation matrix

$$R(\hat{q}_b^e[0]) = I_3 + 2s_q[0]S(r_q[0]) + 2S(r_q[0])^2 \tag{S3}$$

Iteration: k

4: Get $\hat{f}^e[k]$ from the TMO,

5: Get $f_{\text{IMU}}^b[k]$, $\omega_{\text{IMU}}^b[k]$ from the IMU and performing vector calculations,

$$\underline{f}^b = f_{\text{IMU}}^b[k]/\|f_{\text{IMU}}^b[k]\|, \qquad \underline{v_1}^b[k] = \underline{f}^b, \tag{S4}$$

$$\underline{f}^e = \text{sat}_{M_f}(\hat{f}^e[k])/\|\text{sat}_{M_f}(\hat{f}^e[k])\|, \qquad \underline{v_1}^e[k] = \underline{f}^e, \tag{S5}$$

$$\hat{\sigma}_1[k] = \frac{\delta t_{\text{acc}}}{T} k_1[k]\underline{v_1}^b[k] \times R(\hat{q}_b^e[k-1])^{\mathsf{T}}\underline{v_1}^e[k], \tag{S6}$$

6: **if** new magnetometer measurement is available **then**

7:    Get $m_{\text{mag}}^b[k]$ from the magnetometer and performing vector calculations,

$$\underline{m}^b = m_{\text{mag}}^b[k]/\|f_{\text{mag}}^b[k]\|, \qquad \underline{v_2}^b[k] = \underline{f}^b \times \underline{m}^b \tag{S7}$$

$$\underline{m}^e = m^e/\|m^e\|, \qquad \underline{v_2}^e[k] = \underline{f}^e \times \underline{m}^e \tag{S8}$$

$$\hat{\sigma}_2[k] = \frac{\delta t_{\text{mag}}}{T} k_2[k]\underline{v_2}^b[k] \times R(\hat{q}_b^e[k-1])^{\mathsf{T}}\underline{v_2}^e[k], \tag{S9}$$

8: **else**

9:    $\hat{\sigma}_2[k] = 0_{3\times1}$

10: **end if**

11: Calculating the aggregated injection term, $\hat{\sigma}[k] = \hat{\sigma}_1[k] + \hat{\sigma}_2[k]$.

12: Calculating intermediate variables,

$$\hat{\omega}[k] = \omega_{\text{IMU}}^b[k] - \hat{b}_g^b[k-1] + \hat{\sigma}[k], \tag{S10}$$

$$\Omega(\hat{\omega}[k]) = \begin{pmatrix} 0 & -\hat{\omega}^{\mathsf{T}}[k] \\ \hat{\omega}[k] & -S(\hat{\omega}[k]) \end{pmatrix}, \quad \bar{\Omega}(\omega_{ie}^e) = \begin{pmatrix} 0 & -(\omega_{ie}^e)^{\mathsf{T}} \\ \omega_{ie}^e & S(\omega_{ie}^e) \end{pmatrix}, \tag{S11}$$

$$e^{\left(\frac{T}{2}\Omega(\hat{\omega}[k])\right)} = \cos\left(\frac{T}{2}\|\hat{\omega}[k]\|_2\right) I_4 + \frac{T}{2}\text{sinc}\left(\frac{T}{2}\|\hat{\omega}[k]\|_2\right) \Omega(\hat{\omega}[k]), \tag{S12}$$

$$e^{\left(-\frac{T}{2}\bar{\Omega}(\omega_{ie}^e)\right)} = \left(\cos\left(\frac{T}{2}\|\omega_{ie}^e\|_2\right) I_4 + \frac{T}{2}\text{sinc}\left(\frac{T}{2}\|\omega_{ie}^e\|_2\right) \bar{\Omega}(\omega_{ie}^e)\right)^{-1}. \tag{S13}$$

13: Updating attitude estimate,

$$\hat{q}_b^e[k] = e^{\left(\frac{T}{2}\Omega(\hat{\omega}[k])\right)} e^{\left(-\frac{T}{2}\bar{\Omega}(\omega_{ie}^e)\right)} \hat{q}_b^e[k-1]. \tag{S14}$$

14: Carry out gyro bias projection and update gyro bias estimate,

$$\hat{b}_g^b[k] = \hat{b}_g^b[k-1] - Tk_I[k]\hat{\sigma}[k]. \tag{S15}$$

15: Enforcing unit quaternion constraint, $\hat{q}_b^e[k] = \hat{q}_b^e[k]/\|\hat{q}_b^e[k]\|$,

16: Extracting $s_q[k]$ and $r_q[k]$ from $\hat{q}_b^e[k]$ and calculating the rotation matrix

$$R(\hat{q}_b^e[k]) = I_3 + 2s_q[k]S(r_q[k]) + 2S^2(r_q[k]) \tag{S16}$$

   and providing $R(\hat{q}_b^e[k])$ to the TMO.

17: $k \leftarrow k + 1$.

Sidebar 7: Algorithm 2

Algorithm 2 Discrete-time realization of the TMO in direct form.

Require: Initializing the observer.

1: $\hat{p}^e[0] = p_0(\mu(0), l(0), h(0)) \in \mathbb{R}^3$, $\hat{v}^e[0] = v_0 \in \mathbb{R}^3$, $\xi(0) = 0_{3 \times 1}$, where p_0 is the initial position obtained from them initial latitude $\mu(0)$, longitude $l[0]$ and height over the WGS-84 ellipsis $h[0]$ (height over the mean sea level, approximately). v_0 is the initial velocity.

2: $x^-[0] \leftarrow (\hat{p}^e; \hat{v}^e; \xi)$.

Iteration: k,

3: **if** new GNSS measurement is available **then**

4:     **if** tightly coupled integration **then**

5:         update $C[k]$ matrix based on current satellites in line-of-sight

6:     **end if**

7:     Correction is applied,

$$K_d[k] = P^-[k]C[k]^\intercal(C[k]P^-[k]C^\intercal[k] + R[k])^{-1}, \tag{S17}$$

$$x^+[k] = x^-[k] + K_d[k]\left(y[k] - C[k]x^-[k]\right), \tag{S18}$$

$$P^+[k] = (I_{9+l} - K_d[k]C[k])P^-[k]. \tag{S19}$$

8: **else**

$$x^+[k] = x^-[k] \tag{S20}$$

$$P^+[k] = P^-[k] \tag{S21}$$

9: **end if**

10: Calculating

$$\hat{p}^e[k] = x^+(1:3)[k], \tag{S22}$$

$$\hat{v}^e[k] = x^+(4:6)[k], \tag{S23}$$

$$\xi[k] = x^+(7:9)[k], \tag{S24}$$

$$\hat{f}^e[k] = R(\hat{q}^e_b[k])f^b_{\text{IMU}}[k] + \xi[k] \tag{S25}$$

    and providing $\hat{f}^e[k]$ to the attitude observer.

11: Get $R(\hat{q}^e_b[k])$, $\hat{\sigma}[k]$ from the attitude observer,

12: Get $f^b_{\text{IMU}}[k]$ from the IMU,

13: Update $A_d[\text{k}]$, $B_{d,1}[k]$, $B_d[k]$, $D_d[k]$, $u^*[k]$.

14: Propagation in time,

$$x^-[k+1] = A_d[k]x^+[k] + B_{d,1}[k]u^*[k] + D_d[k], \tag{S26}$$

$$P^-[k+1] = A_d[k]P^+[k]A_d^\intercal[k] + B_d[k]Q_d[k]B_d^\intercal[k]. \tag{S27}$$

15: Enforcing symmetry of $P^-[k+1]$,

$$P^-[k+1] = \frac{1}{2}\left(P^-[k+1] + \left(P^-\right)^\intercal[k+1]\right). \tag{S28}$$

16: $k \leftarrow k+1$.

Author Information

Torleiv H. Bryne (torleiv.h.bryne@itk.ntnu.no) received the M.Sc. degree in Engineering Cybernetics from the Norwegian University of Science and Technology, Department of Engineering Cybernetics, in 2013. He is currently pursuing the Ph.D. degree at the same department. His research interests are in the areas of estimation, in particular navigation using nonlinear and stochastic theory. Marine applications are the main focus areas of his research.

Jakob M. Hansen received the M.Sc. in Electrical Engineering from the Technical University of Denmark (DTU) in 2013. Presently he is pursuing his Ph.D. degree at the Department of Engineering Cybernetics, Norwegian University of Science and Technology, with focus on tight integration between INS and GNSS particularly in aviation applications.

Robert H. Rogne received the M.Sc. degree in Engineering Cybernetics from the Norwegian University of Science and Technology, Department of Engineering Cybernetics, in 2008. He has held several engineering positions in the defense, information technology and marine industries, and since 2013 he has been a Ph.D. candidate at the Department of Engineering Cybernetics, NTNU. His research endeavors are focused towards the areas of estimation and fault-tolerance, in particular in marine navigation applications.

Nadezda Sokolova received the Ph.D. degree in 2011 from Norwegian University of Science and Technology (NTNU), where she worked on weak GNSS signal tracking and use of GNSS for precise velocity and acceleration determination. She also holds a M.Sc. degree in Geomatics Engineering from University of Calgary, Canada, and a M.Sc. degree in Space and Aeronautical Engineering from Narvik University College, Norway. Currently, she works as a research scientist at SINTEF ICT, Communication Systems department and adjunct associate professor at the Centre of Excellence on Autonomous Marine Operations and Systems (AMOS), NTNU. Her primary research interests are in the areas of Global Navigation Satellite Systems and their augmentation via inertial and other secondary data sources.

Thor I. Fossen received the M.Sc. degree in Naval Architecture and the Ph.D. in Engineering Cybernetics in 1987 and 1991, both from the Norwegian University of Science and Technology (NTNU). In the period 19891990 he pursued postgraduate studies as a Fulbright Scholar in aerodynamics and flight control at the Department of Aeronautics and Astronautics, University of Washington, Seattle. In 1993 Fossen was appointed as a Professor of Guidance, Navigation and Control at NTNU and he was elected into the Norwegian Academy of Technological Sciences in 1998. Fossen is currently the co-director of the CoE Centre for Autonomous Marine Operations and Systems (AMOS). Fossen is teaching mathematical modeling of aircraft, marine craft, unmanned vehicles and nonlinear control theory. Fossen has authored approximately 300 scientific papers and 5 textbooks including the Wiley textbooks Guidance and Control of Ocean Vehicles and Handbook of Marine Craft Hydrodynamics and Motion Control. He has served as Associate Editor of Automatica. Fossen is one of the co-founders of Marine Cybernetics where he was Vice President of R&D in the period 20022008. A patent for weather optimal positioning control of marine vessels was granted in 1998. This work received the Automatica Prize Paper Award in 2002. In 2008 he received the Arch T. Colwell Merit Award at the SAE 2008 World Congress for a paper entitled "Nonlinear Observer for Vehicle Velocity Estimation". In 2016 Fossen was elevated to IEEE Fellow.

Tor A. Johansen (M.Sc. and Ph.D.) worked at SINTEF Electronics and Cybernetics as a researcher before he was appointed Associate Professor at the Norwegian University of Science and Technology in Trondheim in 1997 and was promoted to Professor in 2001. He has published more than 100 articles in international journals as well as numerous conference articles and book chapters in the areas of control, estimation and optimization with applications in the marine, automotive, biomedical and process industries. In 2002 Johansen co-founded the company Marine Cybernetics AS where he was Vice President until 2008. Prof. Johansen is currently a principal researcher within the Center of Excellence on Autonomous Marine Operations and Systems (AMOS) and director of the Unmanned Aerial Vehicles Laboratory (UAV-Lab), Department of Engineering Cybernetics, Norwegian University of Science and Technology.